Leipzig University
Faculty of Physics and Earth Sciences
Leipzig Institute for Meteorology

# Aerosol profiling with lidar over the Atlantic Ocean during meridional Polarstern cruises

Master Thesis

Stephanie Bohlmann

| | |
|---|---|
| Primary Supervisor: | Prof. Dr. A. Macke |
| Secondary Supervisor: | Dr. Bernhard Pospichal |
| Tutor: | Dr. Holger Baars |

Leipzig, 7 April 2017

# Abstract

The multiwavelength Raman lidar Polly$^{XT}$ has been operated on several expeditions across the Atlantic Ocean aboard the research vessel Polarstern. In this work, the lidar measurements from five Polarstern cruises are presented and two of them, PS95 from Bremerhaven to Cape Town (autumn 2015) and PS98 from Punta Arenas to Bremerhaven (spring 2016), are analysed in detail. The latest setup of Polly$^{XT}$ allows measurements of the marine boundary layer (MBL) due to an additional near-range receiver.

This work starts with an overview of the different aerosol types that occur over the ocean followed by an introduction into the lidar methodology. An overview of the five Polarstern cruises ANT XXVII/4, ANT XXIX/1, PS83, PS95 and PS98 is given and three case studies of the last two cruises are presented and intensively discussed. In the first case, marine conditions were observed near South Africa on the autumn cruise PS95. Values of optical properties within the MBL correlate with typical marine values. A layer of dried marine aerosol, indicated by an increase of the particle depolarisation ratio to about 10% at both wavelengths on the top of the MBL, could be detected. On the same cruise, an almost pure Saharan dust plume was observed near the Canary Islands. On PS98, several layers of Saharan dust partly mixed with biomass-burning smoke could be measured near the Cape Verde Islands. While the MBL was partly mixed with dust in the pure Saharan dust case, an almost marine MBL was observed in the mixed case.

A statistical analysis showed latitudinal differences in the optical properties within the MBL, caused by the downmixing of dust in the tropics and anthropogenic influences in the northern latitudes whereas the optical properties of the MBL in the southern hemisphere correlate with typical marine values. The particle depolarisation ratio of dried marine layers ranged between 4–9%.

Night measurements from PS95 and PS98 were used to illustrate the potential of aerosol classification using lidar ratio, particle depolarisation ratio and Ångström exponent. Lidar ratio and particle depolarisation ratio have been found to be the main indicator for the particle type, the Ångström exponent is rather variable.

# Table of Contents

**1 Introduction** **1**

**2 Aerosol over the Ocean** **5**

**3 Lidar theory** **7**
3.1 Lidar principle and equation . . . . . 7
3.2 Klett-Fernald method . . . . . 9
3.3 Raman method . . . . . 9
3.4 Depolarisation ratio . . . . . 11
3.5 Aerosol classification . . . . . 12

**4 Experiment** **15**
4.1 Polarstern cruises . . . . . 15
4.2 Main instrument: lidar Polly$^{XT}$ . . . . . 16
4.3 Additional data sources . . . . . 19
4.4 Lidar observations on the previous Polarstern cruises . . . . . 20

**5 Results - Part I: Case studies** **29**
5.1 PS95 - Marine aerosol conditions . . . . . 29
5.2 PS95 - Saharan dust . . . . . 33
5.3 PS98 - Mixed aerosol layers . . . . . 36

**6 Results - Part II: Statistical analysis** **41**
6.1 Time series . . . . . 41
6.2 Potential for particle typing . . . . . 49

**7 Summary and conclusion** **53**

**Bibliography** **54**

**List of Figures** **65**

**List of Tables** **67**

**List of Abbreviations** **69**

# Chapter 1

# Introduction

Aerosols, solid or liquid particles dispersed in air, play an important role in the Earth's climate system. By scattering and absorbing solar and terrestrial radiation, aerosols highly affect the radiation fluxes and thus the radiative budget. Besides this direct aerosol radiative forcing, aerosols also modify the microphysical properties of clouds by acting as cloud condensation or ice nuclei, and thereby influence the radiative budget indirectly (Twomey-effect, [*Twomey*, 1977]). Furthermore, the presence of aerosol particles influence the lifetime of clouds (cloud lifetime effect, [*Albrecht*, 1989]).
The impact of aerosols on the climate system is various and has to be considered in climate modelling to receive accurate results. At the same time, information about global aerosol distributions are rare because of their high spatial and temporal variability. Furthermore, not all aerosol types contribute to the aerosol radiative forcing in the same way [*Ocko et al.*, 2012; *Myhre et al.*, 2013]. Uncertainties in aerosol forcing and the poor understanding of aerosol-cloud interactions represent a large uncertainty in current climate models despite the progress in observing and modelling climate-relevant aerosol properties and atmospheric distributions in the last years [*IPCC*, 2013]. More information about the horizontal and vertical distribution of aerosol is needed to further improve climate modelling and prediction. Many studies investigate aerosol distributions over land, but since about 70% of the Earth's surface is covered by water, the investigation of aerosols and their distribution over the ocean is very important as well.
Light detection and ranging (LIDAR) represents a key method to investigate the distribution of aerosols. Measurements with high spatial and temporal resolution and under ambient conditions are possible up to an altitude of 100 km depending on the lidar setup [*Wandinger*, 2005a]. Many institutes all over the world are performing lidar measurements and form networks as shown in Fig. 1.1. Currently 29 stations contribute to the European Aerosol Research Lidar Network (EARLINET)[*Pappalardo et al.*, 2014]. The Commonwealth of Independent States Lidar Network (CISLiNet)[*Chaikovsky et al.*, 2006] and the Asian Dust Network (AD-NET) [*Sugimoto et al.*, 2008] perform measurements all over Asia. The Regional East Aerosol Lidar Mesonet (REALM) [*Hoff et al.*, 2002], replaced by the NOAA Cooperative Remote Sensing Science and Technology (CREST) Lidar Network (CLN), oper-

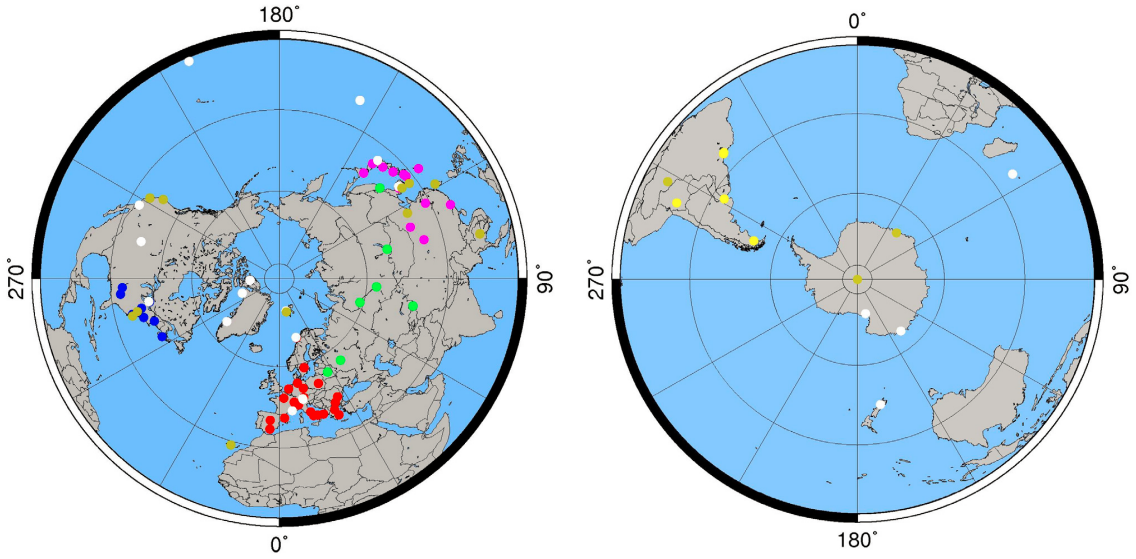


(a) northern hemisphere (b) southern hemisphere

**Figure 1.1:** Lidar stations on northern and southern hemisphere, coloured dots distinguish the different networks: EARLINET (red), AD-NET (violet), ALINE (yellow), CISLiNet (green), MPLNET (brown), NDACC (white) and REALM (blue). Figure taken from *Bösenberg et al.* [2007].

ate lidar facilities on the US American east-coast and the American Lidar Network (ALINE) [*Antuña et al.*, 2012; *Barbosa et al.*, 2014] coordinates lidar measurements in South America. There are also global operating networks like the NASA Micro-Pulse Lidar Network (MPLNET) [*Welton et al.*, 2001] and the Network for the Detection of Atmospheric Composition Change (NDACC) [*Leblanc et al.*, 2016]. While the northern hemisphere is well covered, there are only a few lidar stations on the southern hemisphere. Especially over the oceans almost no measurements of tropospheric aerosol are available. To close this gap, the OCEANET project, a shipborne facility to investigate the transport of material and energy between ocean and atmosphere, was initiated. The OCEANET project is a collective project of several German research institutes (see Sec. 4.1) and combines oceanographic measurements with atmospheric observations. It is regularly part of expeditions on research vessels (RV) like the RV Polarstern. One instrument within the OCEANET facility is the portable Raman and polarization lidar system Polly$^{XT}$ [*Althausen et al.*, 2009; *Engelmann et al.*, 2016]. The first cruise with Polly$^{XT}$ took place in 2009. Since then, eight cruises have been performed on the RV Polarstern between Bremerhaven and Punta Arenas and Bremerhaven and Cape Town until summer 2016. The first three cruises ANT-XXVI/1, ANT-XXVI/4 and ANT-XXVII/1 have already been analysed by *Kanitz* [2012]. Saharan dust and dust and biomass-burning smoke mixtures were measured at the west coast of North Africa as well as Patagonian dust over the South Atlantic. The used lidar system did not cover the lower most 500–800 m of the troposphere and so the marine boundary layer

(MBL) could not be investigated. Polly$^{XT}$ has been further developed since these first cruises. The latest setup possesses four near-range channels and depolarisation measurements at two wavelengths. Furthermore, the height of complete overlap between receiver field-of-view and laser beam was reduced from about 1500 m to 120 m due to a new near-range detection unit and now enables measurements close to the lidar. Observations with this advanced lidar setup over the ocean offer the unique opportunity to investigate not only aerosol conditions in the free troposphere but also in the MBL, which was not possible until now.
On the Polarstern cruise PS95 in November 2015 and the spring cruise PS98 in April/May 2016 the latest Polly$^{XT}$ system was operated within the OCEANET facility. Because of the new possibility to perform measurements close to the lidar with several wavelengths, one focus of this study is the investigation of the MBL in addition to the investigation of free-tropospheric aerosol over the ocean. The two recent cruises PS95 and PS98 are therefore analysed in detail.
After the introduction, a brief overview of the aerosol types occurring over the ocean is given in Chapter 2. In Chapter 3, the principle of lidar systems and the derived optical particle quantities as well as the aerosol classification methodology are introduced. Chapter 4 describes the experiment, i.e. the RV Polarstern and the OCEANET project itself as well as the applied lidar system Polly$^{XT}$ and further data sources. Furthermore, an overview of the lidar observations on the Polarstern cruises ANT XXVII/4, ANT XXIX/1, PS83, PS95 and PS98 is given. Results of the cruises PS95 and PS98 are presented in Chapter 5 and 6. At first, three case studies are discussed. Afterwards, all analysed measurements are presented statistically. A conclusion is given in Chapter 7.

# Chapter 2

# Aerosol over the Ocean

Aerosol over the Atlantic Ocean can either originate directly from the ocean, like sea salt or non-sea-salt sulphate particles, or it can be advected from the continent. The atmospheric lifetime of many terrestrial aerosols like biomass-burning aerosol, dust or anthropogenic fossil fuel combustion aerosol is comparable with the atmospheric transport times across the ocean and thus make an important contribution to the marine aerosol [*Saltzman*, 2009].
An overview of the different aerosol sources over the Atlantic Ocean is given in Fig. 2.1. The main transport paths are indicated by arrows. Biomass-burning aerosol from Canadian forest fires (1) transported across the northern Atlantic towards Europe was measured by *Müller et al.* [2005]. Aerosol from anthropogenic sources in North America (2) [*Russell et al.*, 1999] and Europe (3) [*Ansmann et al.*, 2001] is also transported towards the Atlantic Ocean. Dust from the Saharan desert (4) [*Tesche et al.*, 2011a] and other smaller deserts in southern Africa (7) [*Swap et al.*, 1996] and Patagonia (9) [*Kanitz et al.*, 2013] as well as smoke from biomass burning in the Amazons (6) and central Africa (5) [*Ansmann et al.*, 2009] highly influences the aerosol conditions of the tropical Atlantic. Marine aerosols like sea salt (8) occur all over the ocean where the surface water is swirled up by wind [*Smirnov et al.*, 2002]. As can be seen in Fig. 2.1, sources of aerosols over the Atlantic Ocean are diverse and not only aerosols originated from the ocean contribute to the aerosol composition. Nevertheless, sea salt aerosol emitted from the sea surface into the atmosphere, is one major primary aerosol type [*Andreae and Rosenfeld*, 2008]. Especially in remote ocean regions, the properties of the MBL are strongly influenced by sea salt aerosol and non-sea-salt sulphate particles [*Prospero*, 2002]. The main source of non-sea-salt sulphate particles is the oxidation of dimethyl sulphide (DMS) which is produced by phytoplankton [*Andreae and Raemdonck*, 1983]. Sea salt aerosol is mainly generated by the action of wind on the sea surface. The wind generates waves which break at sufficient high wind speeds, typically $>5\,\mathrm{ms}^{-1}$, and introduce bubbles in the surface water [*Saltzman*, 2009]. These bubbles burst when they reach the sea surface and eject so called film and jet drops into the atmosphere. This process is strongly depending on wind speed which makes the estimation of the sea salt aerosol production very difficult [*Prospero*, 2002].
Another major aerosol component over the Atlantic Ocean is mineral dust. Especially the

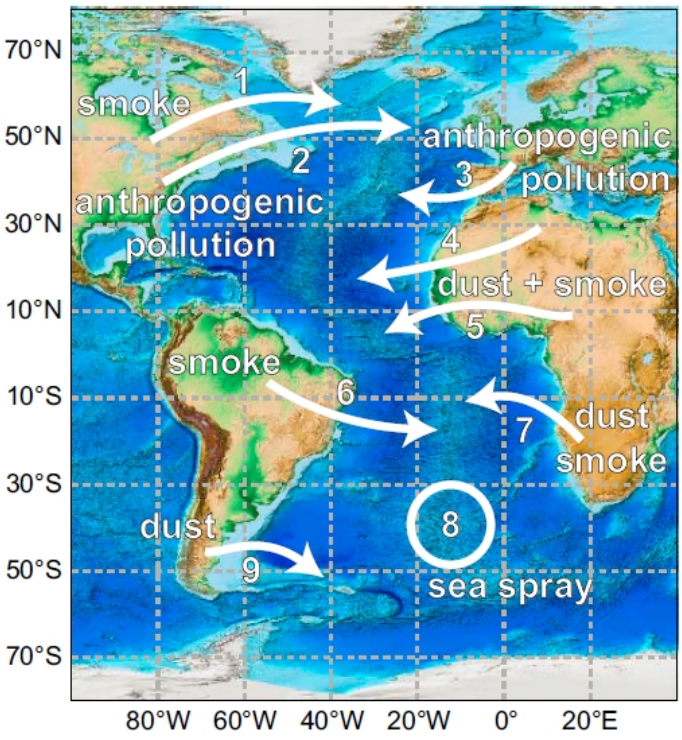


**Figure 2.1:** Aerosol sources and their expected transport direction over the Atlantic Ocean (taken from *Kanitz* [2012]).

northern subtropical and tropical Atlantic is highly influenced by dust from the Saharan desert. Mineral dust is generated in arid regions from the action of wind on the surface and mainly consists of silicates, quartz and carbonates [*Kandler et al.*, 2009]. The particles are uplifted by wind, turbulences or convection and are transported toward the ocean. Because of the large areas dust plumes can cover, the persistence of these plumes and their optical properties, i.e. the scattering and absorbing of solar and terrestrial radiation, dust is one major subject in climate studies and was investigated, e.g. during the Saharan Mineral Dust Experiment (SAMUM)[*Heintzenberg*, 2009] or the Saharan Aerosol Long-range Transport and Aerosol-Cloud-Interaction Experiment (SALTRACE)[*Weinzierl et al.*, 2016].
Organic aerosols like soot from fuel combustion and biomass burning can influence the aerosol composition above the Atlantic Ocean as well. Biomass-burning aerosol (BBA) is generated by wildfires or controlled burning for agriculture mainly in the tropics [*Andreae*, 1991]. Smoke over the Atlantic near Africa was investigated by *Tesche et al.* [2011b]. And even long-range transported African smoke could be observed in the Amazon Basin by *Baars et al.* [2011], *Ansmann et al.* [2009] and *Ben-Ami et al.* [2010].

# Chapter 3

# Lidar theory

LIght Detection And Ranging (LIDAR) represents a method to investigate vertical profiles of atmospheric parameters without manipulating their properties. In this chapter, the principle of optical remote sensing of aerosols with lidar will be introduced as well as the aerosol optical properties themselves. Afterwards, the methodology for aerosol type classification using these properties will be illustrated.

## 3.1 Lidar principle and equation

The principle of lidar systems is based on the emission of monochromatic and coherent laser pulses, which are backscattered in the atmosphere by molecules and particles and detected by a telescope.
The detected signal $P$ at the emission wavelength $\lambda$ is defined by the lidar equation by *Wandinger* [2005a]:

$$P_\lambda(R) = P_0 C_\lambda^s \frac{O(R)}{R^2} \beta_\lambda(R) \exp\left[-2\int_0^R \alpha_\lambda(r)\, dr\right], \tag{3.1}$$

with

$$\beta_\lambda(R) = \beta_\lambda^{par}(R) + \beta_\lambda^{mol}(R) \tag{3.2}$$

and

$$\alpha_\lambda(R) = \alpha_\lambda^{par}(R) + \alpha_\lambda^{mol}(R). \tag{3.3}$$

In principle, light with the power $P_0$ at the wavelength $\lambda$ is emitted into the atmosphere. The range $R$ at which the light is backscattered to the lidar by molecules and particles is given by the time $t$ between emission and detection of the signal with: $R = \frac{c \cdot t}{2}$, where $c$ is the speed of light. The amount of the light, that is backscattered at an angle of 180°, is described by the backscatter coefficient $\beta_\lambda(R)$. It is distinguished between backscattering by particles $\beta_\lambda^{par}$ and by molecules $\beta_\lambda^{mol}$ (Eq. 3.2). On the way through the atmosphere, the emitted light is attenuated due to absorption and scattering. This attenuation is described by the extinction coefficient $\alpha_\lambda(R)$. Again, it is distinguished between the extinction caused

by particles $\alpha_\lambda^{par}$ and molecules $\alpha_\lambda^{mol}$ (Eq. 3.3). The molecular backscatter and extinction coefficient can be estimated from known temperature and pressure profiles [*Bucholtz*, 1995]. The transmission term results from the Bouguer-Lambert-Beer law and indicates the amount of light that gets lost on way through the atmosphere. As the light is attenuated on the way from lidar to the scatterer as well as on the way back, a factor of 2 has to be considered.
Additionally, device typical parameters like pulse length, telescope area and system efficiency are taken into account. These system parameters are described by the height independent system constant $C_\lambda^s$. $O(R)$ describes the overlap between the laser beam and receiver-field-of-view and varies between 0 (no overlap) close to the lidar and 1, which means full overlap. In regions with only partial overlap (0<O(R)<1), the measured signal is affected by this incomplete overlap and an overlap correction may be applied. A detailed explanation of the overlap function is given in *Wandinger and Ansmann* [2002]. Furthermore, the received signal is inversely proportional to $R^2$ because the receiver telescope area is part of the surface of the sphere with radius $R$ that encloses the scattering volume and thus the signal intensity decreases with increasing distance from the lidar. To use the received signal as indicator of the backscattering, it has to be multiplied with $R^2$. The range-corrected signal $P_\lambda(R)\,R^2$ is therefore given by:

$$P_\lambda(R)\,R^2 = P_0 C_\lambda^s O(R)\left(\beta_\lambda^{par}(R)+\beta_\lambda^{mol}(R)\right)\exp\left[-2\int_0^R\left(\alpha_\lambda^{par}(r)+\alpha_\lambda^{mol}(r)\right)dr\right]. \quad (3.4)$$

Equation 3.1 and 3.4 apply for elastic scattering, which means the wavelength is not changed during scattering.
To derive particle backscatter and extinction profiles, two approaches are used to solve the lidar equation. Both are introduced in the following sections. Two parameters, the lidar ratio and the Ångström exponent, are necessary to apply these approaches and furthermore can be indicators of the aerosol type, since the scattering and absorption depends on size, shape, concentration and refractive index of the particles [*Müller et al.*, 1999].
The ratio of extinction to backscatter coefficient is called lidar ratio $S$. The lidar ratio of aerosol particles at the wavelengths $\lambda$ is defined as:

$$S_\lambda^{par}(R) = \frac{\alpha_\lambda^{par}(R)}{\beta_\lambda^{par}(R)}. \quad (3.5)$$

As the extinction is the attenuation of light due to scattering and absorption, the lidar ratio can be used to determine the absorbing capacity of the backscattering particles.
The Ångström exponent $\mathring{A}$ is used to determine the wavelengths dependence of a parameter [*Ångström*, 1929]. It describes the ratio of the parameter at two wavelengths $\lambda_1$, $\lambda_2$ as a function of the ratio of these wavelengths. The Ångström exponent of the extinction coefficient between two wavelengths $\mathring{A}_{ext}^{\lambda_1/\lambda_2}$ is defined as:

$$\frac{\alpha_{\lambda_1}}{\alpha_{\lambda_2}} = \frac{\lambda_2}{\lambda_1}^{\mathring{A}}, \qquad \mathring{A}_{ext}^{\lambda_1/\lambda_2} = \frac{\ln\frac{\alpha_{\lambda_1}}{\alpha_{\lambda_2}}}{\ln\frac{\lambda_2}{\lambda_1}}, \qquad \lambda_2 > \lambda_1. \quad (3.6)$$

The backscatter-related Ångström exponent $\mathring{A}_{bsc}^{\lambda_1/\lambda_2}$ is calculated similar [*Ansmann and Müller*, 2005]. Small particles show a strong wavelength dependence, thus $\mathring{A}$ is greater than 1. In contrast, the scattering on large particles is almost wavelength independent and $\mathring{A}$ is approximately zero [*Eck et al.*, 1999].

## 3.2 Klett-Fernald method

The lidar equation for elastic scattering Eq. 3.1 contains two unknown parameters. By assuming a lidar ratio $S_{\lambda}^{par}$, $\beta_{\lambda_0}^{par}$ can be retrieved with the Klett-Fernald method [*Klett*, 1981; *Fernald*, 1984] by:

$$\beta_{\lambda_0}^{par}(R) = -\beta_{\lambda_0}^{mol}(R) + \frac{A_{\lambda_0}(R_0, R)}{B_{\lambda_0}(R_0) - 2S_{\lambda_0}^{par}\int_{R_0}^{R} A_{\lambda_0}(R_0, r)\, dr}, \tag{3.7}$$

with

$$A_{\lambda_0}(R_0, R) = P_{\lambda_0}(R)\, O(R) R^2 \exp\left[-2\left(S_{\lambda_0}^{par} - S^{mol}\right)\int_{R_0}^{R} \beta_{\lambda_0}^{mol}(r)\, dr\right] \tag{3.8}$$

and

$$B_{\lambda_0}(R_0) = \frac{P_{\lambda_0}(R_0)\, O(R) R_0^2}{\beta_{\lambda_0}^{par}(R_0) + \beta_{\lambda_0}^{mol}(R_0)}. \tag{3.9}$$

Besides the lidar ratio $S_{\lambda_0}^{par}$, a reference height $R_0$ and the backscatter coefficient $\beta_{\lambda_0}^{par}(R_0)$ for this reference height have to be specified. The reference height is supposed to be in a height layer with very small particle scattering compared to the molecular backscattering. The Klett-Fernald method is strongly depending on the overlap function and the assumption of a constant lidar ratio, which can cause large errors [*Sasano et al.*, 1985].

## 3.3 Raman method

Instead of assuming a lidar ratio, the lidar equation can be solved by measuring an additional signal. Equation 3.1 describes the detected signal of the elastic backscattered light, which means there is no energy transfer between particle or molecule and the photon. But during scattering processes, the energy state of the incident photon can be changed if the molecule absorbs energy or transfers energy to the photon. In both cases, the wavelength of the incident photon is shifted and the scattering process is called inelastic or Raman scattering. Raman lidar systems detect the inelastic (Raman) backscattered signal of nitrogen or oxygen molecules in addition to the elastic backscattered signal by air molecules and particles. The Raman backscattered signal $P_{\lambda_{Ra}}(R)$ can be described as [*Wandinger*, 2005b]:

$$P_{\lambda_{Ra}}(R) = P_0 C_{\lambda_{Ra}}^{s} \frac{O_{\lambda_{Ra}}(R)}{R^2} \beta_{\lambda_0}^{Ra}(R) \exp\left[-\int_0^R \left(\alpha_{\lambda_0}(r) + \alpha_{\lambda_{Ra}}(r)\right) dr\right], \tag{3.10}$$

with the Raman backscatter coefficient

$$\beta_{\lambda_0}^{Ra}(R) = N_{Ra}(R)\, \frac{d\sigma_{Ra}}{d\Omega}(\pi, \lambda_0), \tag{3.11}$$

which is given by the molecule number density $N_{Ra}$ and the differential cross section for the backward direction $\frac{d\sigma_{Ra}}{d\Omega}(\pi, \lambda_0)$ of the gas. $N_{Ra}$ can be calculated from known temperature and pressure profiles, provided by radio soundings or GDAS1 data (Sec. 4.3). In contrast to the elastic lidar equation (Eq. 3.1), the extinction on the way back to the lidar has to be considered at the Raman wavelength $\lambda_{Ra}$. Raman wavelengths for the initial wavelengths ($\lambda_0$) 355 nm and 532 nm by inelastic scattering on nitrogen are 387 nm and 607 nm, respectively. The Raman signal from water vapour molecules are detected at 407 nm ($\lambda_0$=355 nm).
Measuring the Raman backscattered signal $P_{\lambda_{Ra}}(R)$, the particle extinction coefficient can be calculated directly by *Ansmann et al.* [1990]:

$$\alpha_{\lambda_0}^{par}(R) = \frac{\frac{d}{dR}\ln\frac{N_{Ra}(R)}{P_{\lambda_{Ra}}(R)R^2/O(R)} - \alpha_{\lambda_0}^{mol}(R) - \alpha_{\lambda_{Ra}}^{mol}}{1 + \left(\frac{\lambda_0}{\lambda_{Ra}}\right)^{\mathring{A}_{ext}}}. \tag{3.12}$$

The particle backscatter coefficient can be calculated using the elastic backscattered signal $P_{\lambda_0}(R)$ and the Raman backscattered signal $P_{\lambda_{Ra}}(R)$ [*Ansmann et al.*, 1992]:

$$\begin{aligned}\beta_{\lambda_0}^{par}(R) = &-\beta_{\lambda_0}^{mol}(R) + \left[\beta_{\lambda_0}^{par}(R_0) + \beta_{\lambda_0}^{mol}(R_0)\right] \\ &\times \frac{P_{\lambda_{Ra}}(R_0)\, P_{\lambda_0}(R)\, N_{Ra}(R)}{P_{\lambda_0}(R_0)\, P_{\lambda_{Ra}}(R)\, N_{Ra}(R_0)} \\ &\times \frac{\exp\left[-\int_{R_0}^{R}\left(\alpha_{\lambda_{Ra}}^{par}(r) + \alpha_{\lambda_{Ra}}^{mol}(r)\right)dr\right]}{\exp\left[-\int_{R_0}^{R}\left(\alpha_{\lambda_0}^{par}(r) + \alpha_{\lambda_0}^{mol}(r)\right)dr\right]}\end{aligned} \tag{3.13}$$

Like for the Klett method, a reference height $R_0$ and the backscatter coefficient $\beta_{\lambda_0}^{par}(R_0)$ in this height have to be defined. In contrast, the extinction coefficient can be determined directly and no assumption of the lidar ratio is necessary. Furthermore, the overlap function cancels out as the ratio of two signals with (ideally) equal overlap behaviour is used for the retrieval of the particle backscatter coefficient. The intensity of the backscattered signal due to nitrogen is much lower than the scattering of daylight on molecules, therefore the Raman method is mostly restricted to nighttime measurements.

Backscatter and extinction coefficient are extensive quantities and thus depend on the particle number. They indicate the amount of light that is backscattered or extinguished. To determine the particle type, intensive quantities, which are independent of particle concentration, are necessary. The intensive optical particle properties are the previously defined lidar ratio and Ångström exponent and the particle depolarisation ratio, which will be introduced in the following section.

## 3.4 Depolarisation ratio

The emitted light of the lidar is linear polarised. In the atmosphere, the light is depolarised while scattered at non-spheric particles like dust or ice crystals. The detected light therefore contains a cross-polarised component $P_\lambda^\perp$ in addition to the parallel polarised light $P_\lambda^\parallel$ (the parallel component determines the light polarised in the same plane as the emitted light):

$$P_\lambda^\perp(R) = P_0 C_\lambda^{s\perp} \frac{O(R)}{R^2} \beta_\lambda^\perp(R) \exp\left[-2\int_0^R \alpha_\lambda(r)\, dr\right] \tag{3.14}$$

and

$$P_\lambda^\parallel(R) = P_0 C_\lambda^{s\parallel} \frac{O(R)}{R^2} \beta_\lambda^\parallel(R) \exp\left[-2\int_0^R \alpha_\lambda(r)\, dr\right]. \tag{3.15}$$

The volume depolarisation ratio is defined as:

$$\delta_\lambda^{vol}(R) = \frac{\beta_\lambda^\perp(R)}{\beta_\lambda^\parallel(R)} = \frac{\beta_\lambda^{mol,\perp}(R) + \beta_\lambda^{par,\perp}(R)}{\beta_\lambda^{mol,\parallel}(R) + \beta_\lambda^{par,\parallel}(R)}. \tag{3.16}$$

The particle and molecular depolarisation ratios are defined analogously:

$$\delta_\lambda^{par}(R) = \frac{\beta_\lambda^{par,\perp}(R)}{\beta_\lambda^{par,\parallel}(R)}, \tag{3.17}$$

$$\delta_\lambda^{mol}(R) = \frac{\beta_\lambda^{mol,\perp}(R)}{\beta_\lambda^{mol,\parallel}(R)}. \tag{3.18}$$

The cross and linear polarised signal components are separated by polarising beam splitters. These beam splitters possess different transmissions for cross and parallel polarised light and thus lead to different transmission efficiencies for cross and parallel polarised light in the detection channel [*Engelmann et al.*, 2016]. The linear depolarisation ratio therefore has to be calibrated. The calibration method applied here, is the $\Delta 90°$ or $\pm 45°$ method explained by *Freudenthaler et al.* [2009]; *Freudenthaler* [2016]. It is based on the determination of a calibration factor $V^*$ from two subsequent measurements with a difference of exactly 90°. The calibration factor is defined as [*Freudenthaler et al.*, 2009]:

$$V^* = \frac{1+T}{1+R}\sqrt{\delta^*(45°) \cdot \delta^*(-45°)}, \tag{3.19}$$

with the receiver transmission ratios of the total and cross-polarized radiation for the total channel $T$ and the cross-polarised channel $R$ (Polly$^{\mathrm{XT}}$- OCEANET: $T$=0.69, $R$=500 at 355 nm and $T$=1.09, $R$=500 at 532 nm). $\delta^*(\pm\varphi)$ is the ratio of the cross-polarized and the total signal at an angle $\varphi$ between the polariser plane and polarisation plane of the laser. Three times a day, a polariser sheet is automatically rotated in the light path, to position the polariser in an angle of $+45°$ and $-45°$ with respect to the polarisation plane of the

laser and measure the signal ratio of the cross to parallel polarised light at ±45°. This methodology has shown, that $V^*$ stays usually constant unless the neutral density filters are changed. With the signal ratio at an angle of 0° between the plane of the polariser and the polarisation plane of the laser $\delta^*(0°) = \frac{P_{532s}}{P_{532g}}$, the calibration factor $V^*$ and the transmission ratios $T$ and $R$, the volume depolarisation can be calculated by:

$$\delta^{vol} = \frac{1 - \frac{\delta^*(0°)}{V^*}}{\frac{\delta^*(0°)}{V^*}T - R}. \tag{3.20}$$

The particle depolarisation ratio then is calculated after *Mattis* [2002]:

$$\delta_\lambda^{par}(R) = \left[\delta_\lambda^{vol}(R) + 1\right]\left(\frac{\beta_\lambda^{mol}(R)\left[\delta_\lambda^{mol}(R) - \delta_\lambda^{vol}(R)\right]}{\beta_\lambda^{par}(R)\left[1 + \delta_\lambda^{mol}(R)\right]} + 1\right)^{-1} - 1, \tag{3.21}$$

using the particle and molecular backscatter coefficients, the volume depolarisation ratio and the linear depolarisation ratio for molecules $\delta^{mol}$, which is determined in a particle free region of the atmosphere.
The particle depolarisation ratio is an intensive quantity and enable the determination of the particle sphericity. If the backscattering particles are mainly spherical, the particle depolarisation ratio is about zero because the linear polarised light has been reflected to the lidar without depolarisation within the particle or its edges. The particle depolarisation ratio increases with non-spherical shape.

## 3.5 Aerosol classification

By knowing typical values of the lidar ratio, Ångström exponent and particle depolarisation ratio, the optical dominant particle type can be specified.
The lidar ratio can be used as indicator of the absorbing capacity of the backscattering particles, whereas the Ångström exponent describes the backscatter or extinction at different wavelengths and therefore indicates the particle size. The lidar ratio of absorbing aerosols like soot is much higher than of non-absorbing particles like sea salt. The larger the particle, the smaller the Ångström exponent. The particle depolarisation ratio characterise the particle sphericity. Humid marine aerosol and soot are nearly spherical and therefore have a low particle depolarisation ratio. In contrast, dust is very non-spherical and possesses large particle depolarisation ratios.
Figure 3.1 shows an example of the aerosol classification by the use of the lidar ratio and the particle depolarisation ratio at 355 nm. The measurements were performed with the Raman-polarization lidar POLIS (University of Munich, marked by dots) and Polly$^{\mathrm{XT}}$ (open squares). Dusty mixtures, dust and smoke and pure dust were observed during measurements over Cape Verde [*Groß et al.*, 2011] and over the North Atlantic [*Kanitz et al.*, 2013]. Pure Saharan dust shows a particle depolarisation ratio of 24–27% at 355 nm and lidar ratios of 50–60 sr. Values for dusty mixtures and dust and smoke mixtures differ from the values of

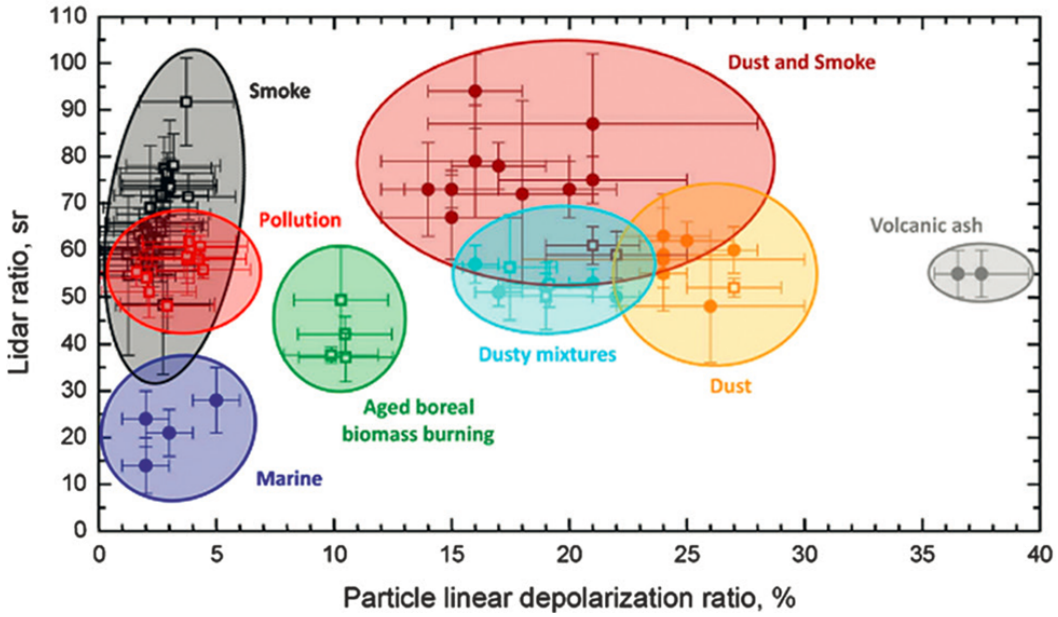


**Figure 3.1:** Aerosol classification by measurements of lidar ratio and particle linear depolarisation ratio at 355 nm, performed with the Raman-polarization lidar POLIS (University of Munich, dots) and Polly$^{XT}$ (TROPOS, open squares). Figure taken from *Illingworth et al.* [2015].

pure dust, depending on the amount of dust and other particles in the mixture. The particle depolarisation ratio of dusty mixtures ranges between 16–22%, whereas the lidar ratios are nearly in the same range as for pure dust. Lidar ratios of dust and smoke mixtures are significantly higher than of pure dust or other dusty mixtures and vary between 60–95 sr.
Pure smoke was measured in the Amazon Basin [*Baars et al.*, 2012] and is characterised by a low particle depolarisation ratio ($\delta^{par} < 5\%$), whereas the lidar ratio range between 50–80 sr. Marine conditions could be observed during the SAMUM-2 campaign over the Cape Verde Islands. Lidar ratios of 14–24 sr and a particle depolarisation ratio of 1–3% were measured for marine aerosol [*Groß et al.*, 2011].
To improve the aerosol classification, the Ångström exponent can be used to gain information about the particle size. Furthermore, geographical location and trajectories can be considered to determine the origin of the particles. An overview of aerosol properties derived in selected previous campaigns is given in Tab. 3.1.

| Measurement site | $S_{355}$[sr] | $S_{532}$[sr] | Å$_{ext}$ | $\delta^{par}_{355}$[%] | $\delta^{par}_{532}$[%] | Reference |
|---|---|---|---|---|---|---|
| **Saharan Dust** | | | | | | |
| Morocco (1) | 53±7 | 55±7 | 0.1±0.2 | 26±6 | 31±3 | *Freudenthaler et al.* [2009]; *Tesche et al.* [2009b] |
| Cape Verde (2a) | 58±7 | 62±5 | | 25±3 | 30±1 | *Groß et al.* [2011] |
| Cape Verde (2b) | 53±10 | 54±10 | 0.2±0.3 | | 31±10 | *Tesche et al.* [2011a] |
| near Cape Verde | 50–60 | 50–60 | 0.1±0.2 | | | *Kanitz et al.* [2013] |
| Leipzig | 55±6 | 50±5 | 0.1±0.4 | | 27±4 | *Baars et al.* [2016] |
| **Polluted Saharan dust** | | | | | | |
| Portugal | 52±20 | 51±11 | 0.4±1.2 | | 13±6 | *Preiler et al.* [2013] |
| Warsaw | 55±20 | 70±10 | 0.5±0.1 | | 20±5 | *Janicka et al.* [2016] |
| Leipzig | 53±3 | | | 19±11 | | *Illingworth et al.* [2015] |
| **Biomass-burning aerosol (BBA)** | | | | | | |
| Cape Verde (2a) | 87±17 | 79±17 | 1.2±0.3 | | 5±2 | *Tesche et al.* [2011b] |
| Amazon(aged) | 62±12 | 64±15 | 1.2±0.4 | 2.5±1 | | *Baars et al.* [2012] |
| South Africa | 89±20 | 83±23 | 1.8±0.5 | | | *Giannakaki et al.* [2015] |
| **Saharan dust – BBA mixture** | | | | | | |
| near Cape Verde | 64±8 | 50±5 | 0.1±0.3 | 22±1 | 26±1 | *Kanitz et al.* [2014] |
| West of Africa | 61±4 | 45±11 | 0.7±0.3 | 21±2 | | *Kanitz et al.* [2013] |
| Cape Verde (2a) | 75±9 | 69±8 | | 18±3 | 16±1 | *Groß et al.* [2011] |
| **Marine aerosol** | | | | | | |
| Cape Verde (2a) | 18±4 | 18±2 | | 2±1 | 2±2 | *Groß et al.* [2011] |
| Portugal (ACE-2) | | 23±3 | 0.3±0.1 | | | *Müller et al.* [2007] |

**Table 3.1:** Aerosol optical properties derived in previous campaigns: lidar ratio $S$ at 355 nm and 532 nm, extinction-related 355/532 nm Ångström exponent and particle depolarisation ratio at 355 nm and 532 nm. SAMUM-1 is denoted by 1, SAMUM-2a = 2a and SAMUM-2b = 2b.

# Chapter 4

# Experiment

## 4.1 Polarstern cruises

One possibility to investigate aerosol over the oceans are measurements aboard research vessels like the German research vessel Polarstern. Besides permanent atmospheric measurements such as air temperature and humidity measurements, which were performed on every cruise, mobile measurement facilities like the OCEANET container are regulary part of the expedition program. The OCEANET project is a combined project of the Alfred Wegener Institute (AWI), the Leibniz Institute for Tropospheric Research (TROPOS), the Helmholtz Centre for Ocean Research (GEOMAR) and the Helmholtz Centre Geesthacht to investigate the transport of material and energy between ocean and atmosphere and to provide atmospheric data in regions where information is rare. Since 2009, the OCEANET project takes regularly part on the spring and autumn Polarstern transit cruises between Bremerhaven and Punta Arenas and Bremerhaven and Cape Town. The RV Polarstern and the OCEANET container are presented in Fig. 4.1. Several meteorological measurement instruments are mounted on the roof of the container. Besides the multiwavelength Raman-lidar Polly$^{XT}$, which is focused in this thesis, a microwave radiometer (HATPRO), a shadowband radiometer, a pyranometer and pyrgeometer and standard meteorological instruments were operated.
Until May 2016, eight Polarstern cruises with the multiwavelength Raman lidar Polly$^{XT}$ aboard have been made. All previous Polly$^{XT}$ Polarstern cruises are listed in Table 4.1, which also gives information on the used lidar (see following section). The cruise tracks are presented in Fig. 4.2. During ANT-XXVII/4 and PS98 the container was located on the observation deck (A in Fig. 4.1). On ANT-XXIX/1, PS83 and PS95 the container was located on the helicopter deck (B in Fig. 4.1). The first three cruises with Polly$^{XT}$ (ANT-XXVI/1, ANT-XXVI/4, ANT-XXVII/1) were already analysed by *Kanitz* [2012].


**Figure 4.1:** Left: Location of the OCEANET container on the observation deck (A) and on the helicopter deck (B) of RV Polarstern. Right: the OCEANET container.

| Cruise label | Time period | Route | Lidar system |
|---|---|---|---|
| ANT-XXVI/1 | 16 Oct - 25 Nov 2009 | BHV - Punta Arenas | Polly$^{XT}$-IfT |
| ANT-XXVI/4 | 7 Apr - 17 May 2010 | Punta Arenas - BHV | Polly$^{XT}$-IfT |
| ANT-XXVII/1 | 27 Oct - 25 Nov 2011 | BHV - Cape Town | Polly$^{XT}$-IfT |
| ANT-XXVII/4 | 20 Apr - 20 May 2011 | Cape Town - BHV | Polly$^{XT}$-IfT |
| ANT-XXIX/1 | 26 Oct - 26 Nov 2012 | BHV - Cape Town | Polly$^{XT}$-OCEANET |
| PS83 | 8 Mar - 12 Apr 2014 | Cape Town - BHV | Polly$^{XT}$-OCEANET |
| PS95 | 29 Oct - 1 Dec 2015 | BHV - Cape Town | Polly$^{XT}$-OCEANET |
| PS 98 | 10 Apr - 12 May 2016 | Punta Arenas - BHV | Polly$^{XT}$-OCEANET |

**Table 4.1:** All previous Polarstern cruises with Polly$^{XT}$ aboard. BHV stands for Bremerhaven. From PS83 a new numbering was used. The used Polly$^{XT}$ type is given as well, for details refer to *Engelmann et al.* [2016].

## 4.2 Main instrument: lidar Polly$^{XT}$

The lidar measurements during the Atlantic cruises were performed with the portable Raman and polarization lidar system Polly$^{XT}$. Ten different Polly$^{XT}$ systems exist by now, all differing slightly in optical setup and capabilities. Figure 4.3 shows the optical setup of Polly$^{XT}$-OCEANET, which was operated on the most of the recent cruises. The emitter units are labelled with the index E, whereas R1–R3 are receiver elements. The whole device is tilted by 5° to avoid specular reflections from horizontally aligned ice crystals [*Seifert et al.*, 2010]. The Nd:YAG laser (E1) emits light pulses at 1064 nm with a repetition frequency of 20 Hz. Two mirrors direct the laser beam through the second and third harmonic oscillator (E2), where light pulses with doubled and tripled frequency (532 and 355 nm) are generated. The linear polarisation of the emitted light at all three wavelengths is ensured by the Brewster-cut Glan-laser polariser (E3) before it is directed upwards by two prisms. A shutter

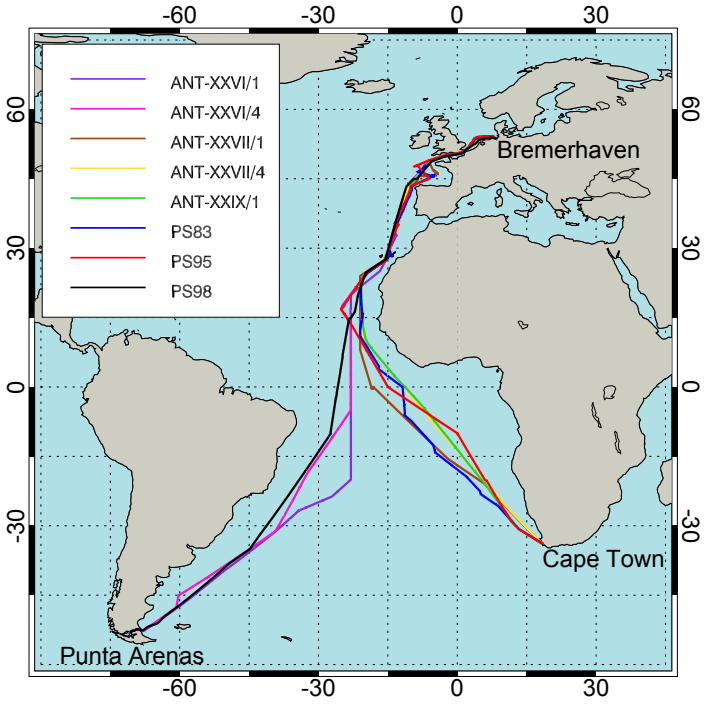


**Figure 4.2:** Polarstern cruises with Polly$^{XT}$ aboard. Cruise tracks are taken from the Pangaea database (`https://www.pangaea.de/expeditions/cr.php/Polarstern`, accessed: 24/02/2017).

(E4) enables the interruption of the light emission, e.g. during airplane overflights without turning off the laser. Before the light pulses at 355, 532 and 1064 nm are emitted into the atmosphere, the beam diameter is enlarged from 7 mm to 45 mm by an achromatic beam expander (E5). In the atmosphere, the emitted light interacts with particles and molecules. The part of the light that is scattered backward is collected by a Newtonian telescope (R2). Through a pinhole (R3), the received light is directed into the detection unit where it is split by dichroic beam splitters depending on its wavelength. Finally, the photons of the individual wavelengths are directed towards the photo multiplier tubes (PMT), which are connected with the data processing unit. Neutral density filters are mounted in front of each PMT to reduce the maximum counting rate and protect the PMTs from overloading. Photons are counted at 355 nm, 387 nm, 407 nm, 532 nm, 607 nm and 1064 nm. Additionally, only the cross-depolarised light at 355 nm and 532 nm is detected by applying polarisers in front of the 355 nm and 532 nm channel (see Sec. 3.4).

To lower the height of partial and complete overlap, a second telescope, shown in the upper part of Fig. 4.3, with a field-of-view of 2.2 mrad is added to the system. The second telescope (R1) allows the measurement of particles closer to the instrument. In Fig. 4.4, the laser beam and the receiver-field-of-view for one telescope (a) and two telescopes with different field-of-views (b) are schematically illustrated. Due to the second telescope the height of complete overlap (O(R)=1) is reduced from about 900 m of the far-range receiver to about 120 m of the near-range receiver and measurements from near the ground up to the tropopause are

possible [*Engelmann et al.*, 2016]. A more detailed description of the optical setup can be found in *Althausen et al.* [2009] and *Engelmann et al.* [2016].
On the cruises ANT-XXVI/1, ANT-XXVI/4, ANT-XXVII/1 and ANT-XXVII/4 (see Table 4.1), a different system, Polly$^{XT}$-IfT, without a near-range channel, a vertical resolution of 30 m and with only one depolarisation channel at 355 nm was used. Since ANT-XXIX/1, depolarisation measurements at 532 nm and 355 nm are performed and near-range channels at 532 nm and 607 nm were added to the Polly$^{XT}$-OCEANET system. Furthermore, the height resolution was increased to 7.5 m. Further information on the different Polly$^{XT}$ systems can be found in *Engelmann et al.* [2016]. On PS95 and PS98, near-range measurements were performed at 532 nm, 607 nm, 355 nm and 387 nm, which enable the observation and the height-resolved characterisation of the MBL at 355 nm and 532 nm, which has never been done before.

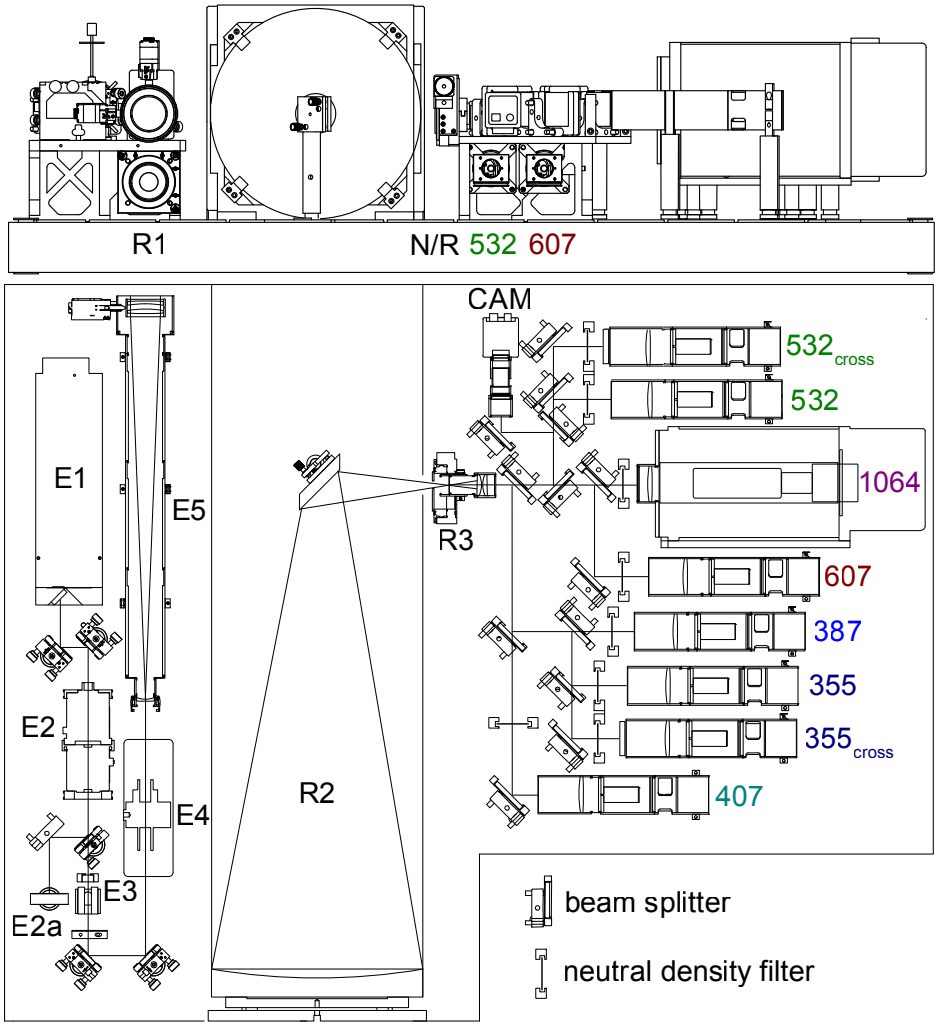


**Figure 4.3:** Optical setup of Polly$^{XT}$. The lower part illustrates the frontal view, the upper part represents the top view. Explanation in the text. Figure taken from *Engelmann et al.* [2016].

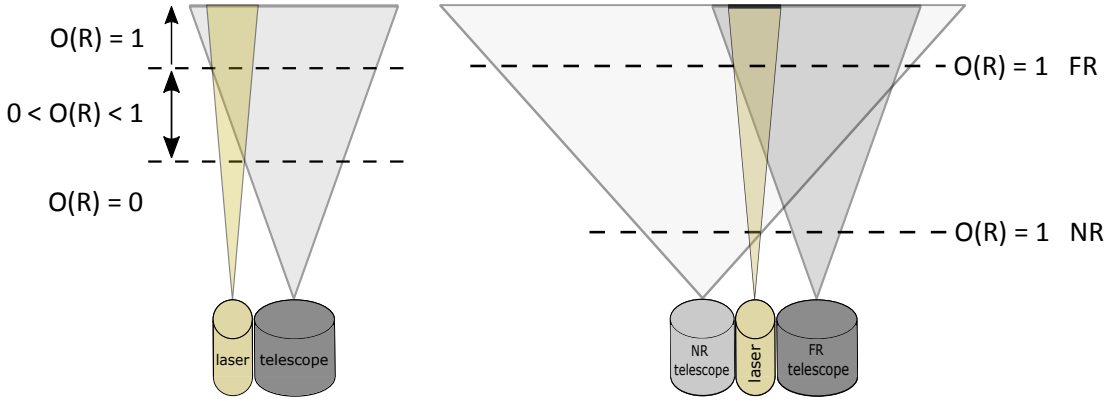


(a) Overlap height without NR telescope (b) Overlap height of NR and FR telescope

**Figure 4.4:** Illustration of the overlap effect for far-range (FR) and near-range (NR) receiver. a) lidar system with far-range telescope only. b) lidar system with far- and near field receiver. O(R) represents the overlap function.

## 4.3 Additional data sources

### Radio sounding and GDAS

Temperature and pressure profiles are necessary to calculate the Rayleigh (molecular) scattering parameter for the lidar data analysis. Temperature and humidity profiles are furthermore used to illustrate trends in the atmosphere associated with particle properties in the following case studies.

Aboard Polarstern, daily balloon soundings provide profiles of temperature, pressure, humidity and horizontal wind direction and velocity. These soundings are normally performed once a day at around 10 UTC and when possible simultaneously with satellite overflights to support comparative studies. The meteorological parameters were measured every five seconds, resulting in a vertical resolution of about 25-50 m [*König-Langlo*, 2016]. Since radio soundings aboard Polarstern were only performed once a day and the vessel is constantly moving, the radio sounding data is often not comparable with meteorological conditions in the night and thus can not be used straightforward for night time measurement analysis. Therefore GDAS1 data was used. GDAS (Global Data Assimilation System) is an atmospheric model provided by the National Centers for Environmental Prediction (NCEP), which provides meteorological parameters like temperature, relative humidity and the wind vector and velocity for 23 altitudes from 1000 to 20 hPa. It assimilates measurement data, e.g. from surface observations, satellite observations or radio soundings like the radio soundings aboard Polarstern, to a gridded model space to initialise weather forecasts with observed data (`https://www.ncdc.noaa.gov/data-access/model-data/model-datasets/global-data-assimilation-system-gdas`, accessed: 24/02/2017). GDAS1 data is calculated every 3 hours for every grid point with a spatial resolution of 1 degree latitude-longitude.

For the observations aboard Polarstern, GDAS1 data was calculated along the cruise track for the nearest grid point.

### HYSPLIT backward trajectories

To determine possible particle sources for the layers investigated in the case studies, backward trajectories were calculated with the Hybrid Single-Particle Lagrangian Integrated Trajectory (HYSPLIT) model. The HYSPLIT model is operated by the National Oceanic and Atmospheric Administration (NOAA) Air Resources Laboratory (ARL) and provides simple air parcel trajectories as well as complex transport, dispersion, chemical transformation and deposition simulations [*Stein et al.*, 2015] using meteorological data, e.g. from GDAS. Further information can be found in *Stein et al.* [2015]. Access to HYSPLIT data is provided via the NOAA ARL READY website: `http://www.arl.noaa.gov/HYSPLIT.php`.
The trajectory calculations in this study were initialised with GDAS1 data. The vertical motion was calculated using the vertical velocity from the meteorological data.

### Microtops sun photometer

During all cruises, except PS81, the aerosol optical thickness (AOT) was measured in the framework of the Maritime Aerosol Network (MAN), which is part of the Aerosol Robotic Network (AERONET).
All measurements were performed with Microtops II sun photometers. These hand-held sun photometers measure the direct solar irradiance at five selected wavelengths (380 nm, 440 nm, 500 nm, 675 nm and 870 nm). The AOT can be derived according to the Bouguer-Lambert-Beer law using the solar radiation at the top of the atmosphere and the measured direct solar irradiance. The solar irradiance at the top of the atmosphere can be calculated with the exact time and location measured by a GPS unit connected with the sun photometer. As the AOT is derived from the attenuation of the solar radiation due to aerosols only, clouds need to be avoided and only measurements under clear sky conditions are viable. To assure data quality, the measured data (Level 1) is screened for clouds and pointing errors and stored as Level 1.5 data. After calibrations and manual inspection the data is stored as quality-assured Level 2.0 data and can be downloaded from the AERONET MAN website: `http://aeronet.gsfc.nasa.gov/new_web/maritime_aerosol_network.html`. In this thesis only Level 2.0 data is used.

## 4.4 Lidar observations on the previous Polarstern cruises

In this section, an observational overview of the five cruises ANT XXVII/4, ANT XXIX/1, PS83, PS95 and PS98 are presented. To give an overview of the measured lidar data, the height-time plots of the 1064 nm range-corrected signal and the 532 nm volume depolarisation ratio are shown in Fig. 4.5 to Fig. 4.9. During ANT XXVII/4 and PS98, the 1064 nm PMT had a technical failure and no measurements at this wavelength were possible. For these

cruises, the 532 nm range-corrected signal is shown instead, which contains a much larger molecular scattering contribution than the 1064 nm signal. In addition, the cruise tracks and the daily averaged AOT at 500 nm and the Ångström exponent (440/870 nm) derived from Microtops sun photometer measurements are given.

### ANT XXVII/4

The expedition ANT XXVII/4 started on 20 April 2011 in Cape Town and ended on 20 May 2011 in Bremerhaven. Figure 4.5 shows the range corrected signal and volume depolarisation ratio at 532 nm. On this cruise, the older Polly$^{XT}$-IfT system was aboard Polarstern. Thus no near-range channels and only the depolarisation ratio at 532 nm were available. Because of a technical failure of the 1064 nm channel, there are no measurements at this wavelength. With some interruptions, measurements could be performed from 26 April to 17 May. From 26 April till 7 May and around the 12 May, lofted aerosol layers were observed. Around the 6 May (15°N) and 12 May (34°N), the higher volume depolarisation ratio indicates the presence of dust.
Throughout the whole cruise the AOT at 500 nm was relatively constant and ranged around 0.1 and 0.2. Exceptions are the 5 and 12 May, on these days the AOT was around 0.3 indicating optical thicker aerosol layers.

### ANT XXIX/1

Between 26 October and 26 November 2012, the Polarstern transit cruise ANT XXIX/1 from Bremerhaven to Cape Town took place. On this cruise, an expanded dust plume in the northern tropics and nearly constant overcast conditions on the southern hemisphere were observed (Fig. 4.6). From 3 November (30°N) complex aerosol layers were measured up to 5 km until 12 November 2012 (6°N). In the first three days, embedded clouds occurred at the top of the aerosol layers. After crossing the equator on 14 November Polarstern left the region of dust and low level clouds below 1 km height occurred frequently. Approaching Cape Town the cloud base height increase to around 2.5 km.

### PS83

Figure 4.7 shows the spring cruise PS83 from Cape Town back to the home port Bremerhaven from 8 March to 12 April 2014. During the first cruise leg, clouds below 2 km occurred frequently. Since the afternoon of 16 March, dust layers between 1.5 and 3.5 km could be detected, which can be seen in the range corrected signal (1064 nm) and the volume depolarisation ratio (532 nm). Until 22 March, the dust top height increased to around 4 km. At the same time, the dust bottom height decreased so that the maximal dust layer thickness was measured on 22 March (7°N). Then, the dust top height suddenly decreased from around 4 km down to 1.7 km and stayed constant for the following days. In the evening of 25 March (16°N), Polarstern temporary left the region of dust before it could be measured again until the morning of 28 March. Near Las Palmas on 30 and 31 March (around 29°N),

last minor traces of dust could be observed before Polarstern finally left the dust region and entered the anthropogenic influenced European region.
On the southern hemisphere, the AOT at 500 nm was low and ranged around 0.05. The maximum was reached on 22 March (7°N) with an AOT of 0.47. In the northern hemisphere, the AOT decreased to around 0.1. A slight increase to around 0.15 at the end of the cruise near Bremerhaven could be observed.

### PS95

The autumn transit cruise PS95 is shown in Fig. 4.8. Polarstern departed on 29 October 2015 from Bremerhaven and arrived on 1 December 2015 at Cape Town. The first days of this cruise were characterised by low-level clouds and rain. On 9 November (33°N), the lidar could detect a lofted plume of Saharan dust above the MBL between 600 m and 3 km height. From 12 November (24°N), increasing depolarisation in the MBL could be observed resulting from deposition and downmixing of dust from higher altitudes. The dust top height decreased from 2.8 km on 11 November down to 1.5 km on 13 November. About noon on 14 November 2015, a new dust plume with a lower volume depolarisation ratio and a dust top height of 3.5 km was observed. Polarstern steadily moved towards the equator so that the dust region was left behind in the night to 18 October (3°N). After entering the southern hemisphere on 19 November, marine stratocumulus clouds occurred frequently. Around noon on 23 November (10°S), minor traces of dust between 1 km and 4 km could be observed again. Considering HYSPLIT trajectories (not shown), these depolarising layers could consist of dust from the Kalahari Desert. From 24 November (12°S), mostly overcast sky was predominant. At the end of the cruise, on 29 and 30 November, almost pure marine conditions could be observed. These measurements will be discussed later in Sec. 5.1.
The 500 nm AOT ranged around 0.1 on the northern hemisphere, increased in the dust influenced northern tropics to around 0.5 and decreased below 0.1 in the southern hemisphere.

### PS98

The spring transit cruise PS98 started on 11 April 2016 in Punta Arenas (Chile) and ended on 11 May 2016 in Bremerhaven. The cruise track and the time series of the range corrected signal and volume depolarisation ratio at 532 nm are shown in Fig. 4.9. After starting regular measurements in the night to 13 April, the weather was dominated by clouds. In the night from 14 to 15 April (40°S), thin depolarising layers at around 2.5 km could be observed. According to HYSPLIT backward trajectories (not shown), the airmass originated from the Patagonian region, thus the layers could contain traces of Patagonian dust. Observations on 16 and 17 April were dominated by low clouds and rain. From 22 April (12°S) to 25 April (4°S), the lidar could detect a lofted plume of Saharan dust between 1.5 km and 3.5 km height. Crossing the Intertropical Convergence Zone (at around 5°N) on the 27 and 28 April, thunderstorms, rain showers and clouds with low base heights were predominant. After leaving this region, the lidar observed Saharan dust above the marine boundary layer

again. The bottom height of the dust layer decreased from 1.5 km on 22 April down to around 600 m on 30 April. In the afternoon of 1 May (23°N), Polarstern left the dust region. After a short stop at the port of Las Palmas (Gran Canaria, Spain) on 3 May, the cruise was continued towards the European continent and the aerosol conditions were more and more influenced by anthropogenic sources. From 6 May, mostly overcast sky with small cloud gaps was predominant.
The AOT at 500 nm showed a similar latitudinal behaviour as on the PS95 cruise. The AOT at 500 nm was below 0.1 in the southern hemisphere, except for the 17 April, and steadily increased to the maximum of 0.37 on 30 April. After leaving the dust influenced region, the AOT ranged between 0.1–0.2 on the northern hemisphere.

### Summary

Regular cruises across the Atlantic Ocean from North to South in autumn and from South to North in spring provided a large amount of lidar data over the Atlantic Ocean. Dust is regularly observed in the northern tropics and subtropics west of the Saharan desert. The AOT at 500 nm, measured with a Microtops sun photometer, is slightly higher on the northern than on the southern hemisphere which indicates a higher aerosol load on the northern hemisphere. This aerosol probably originate from the European continent. On the southern hemisphere, pure marine conditions can be measured. Until now, very few pure marine conditions were detected because of the frequent cloud occurrence in the southern hemisphere.

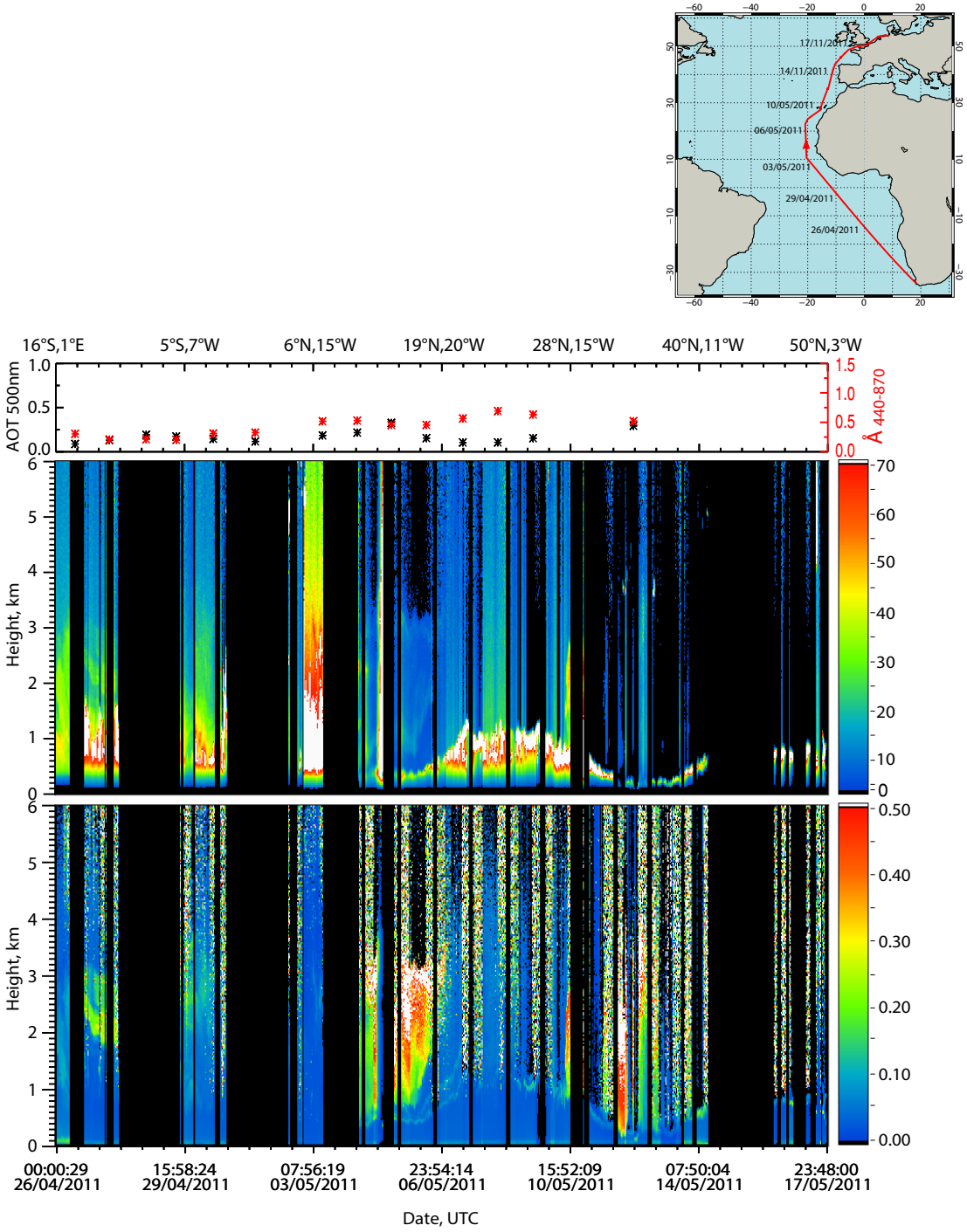


**Figure 4.5:** Observational overview of ANT XXVII/4. Top: cruise track, below: sun photometer derived 500 nm AOT and 440/870 nm backscatter-related Ångström exponent, below: 532 nm range-corrected signal, bottom: 532 nm volume depolarisation ratio. Coordinates mark the position of Polarstern at the given time.

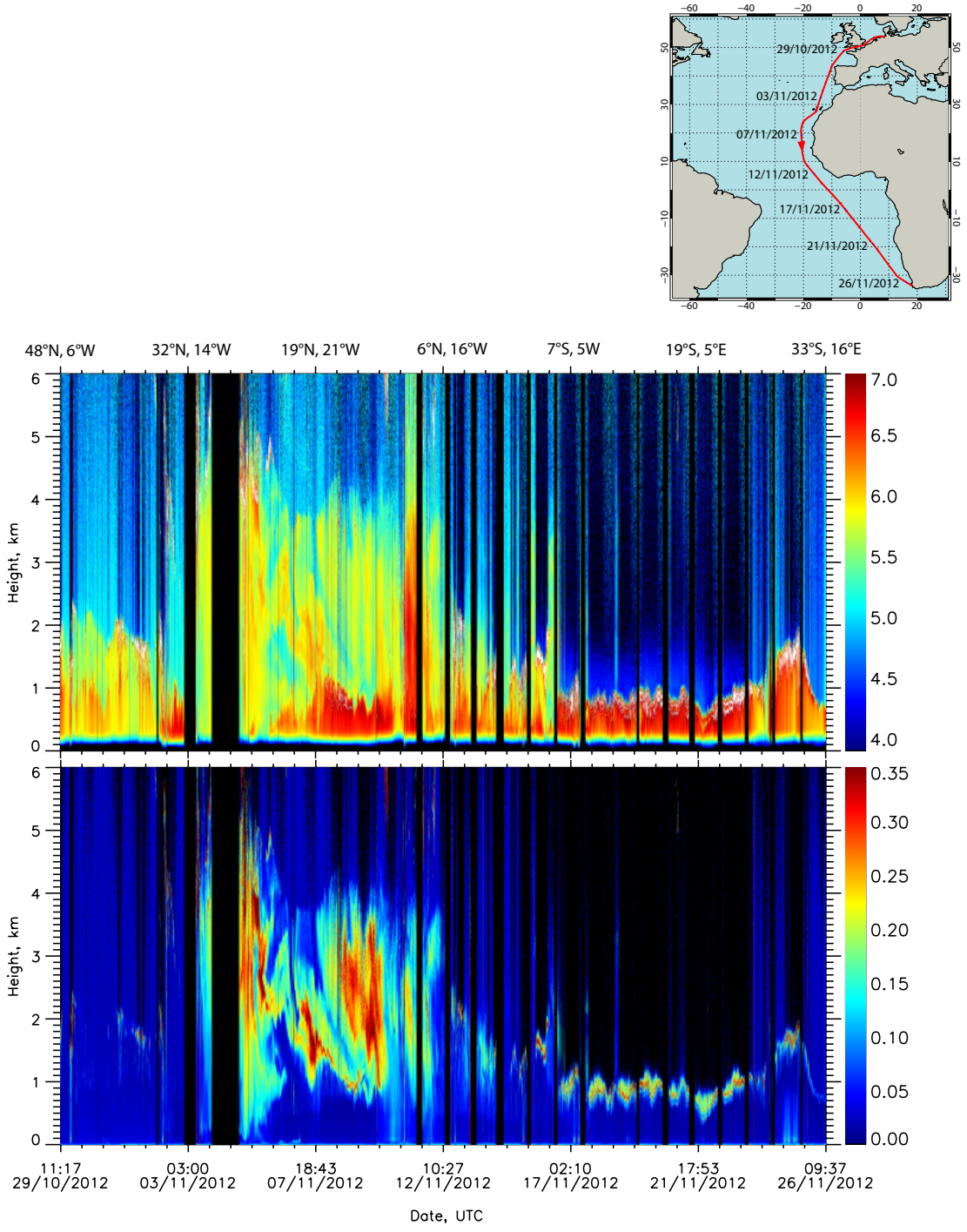


**Figure 4.6:** Observational overview of ANT XXIX/1. Top: cruise track, below: 1064 nm range-corrected signal, bottom: 532 nm volume depolarisation ratio. Coordinates mark the position of Polarstern at the given time. On this cruise, no Microtops sun photometer measurements were performed.

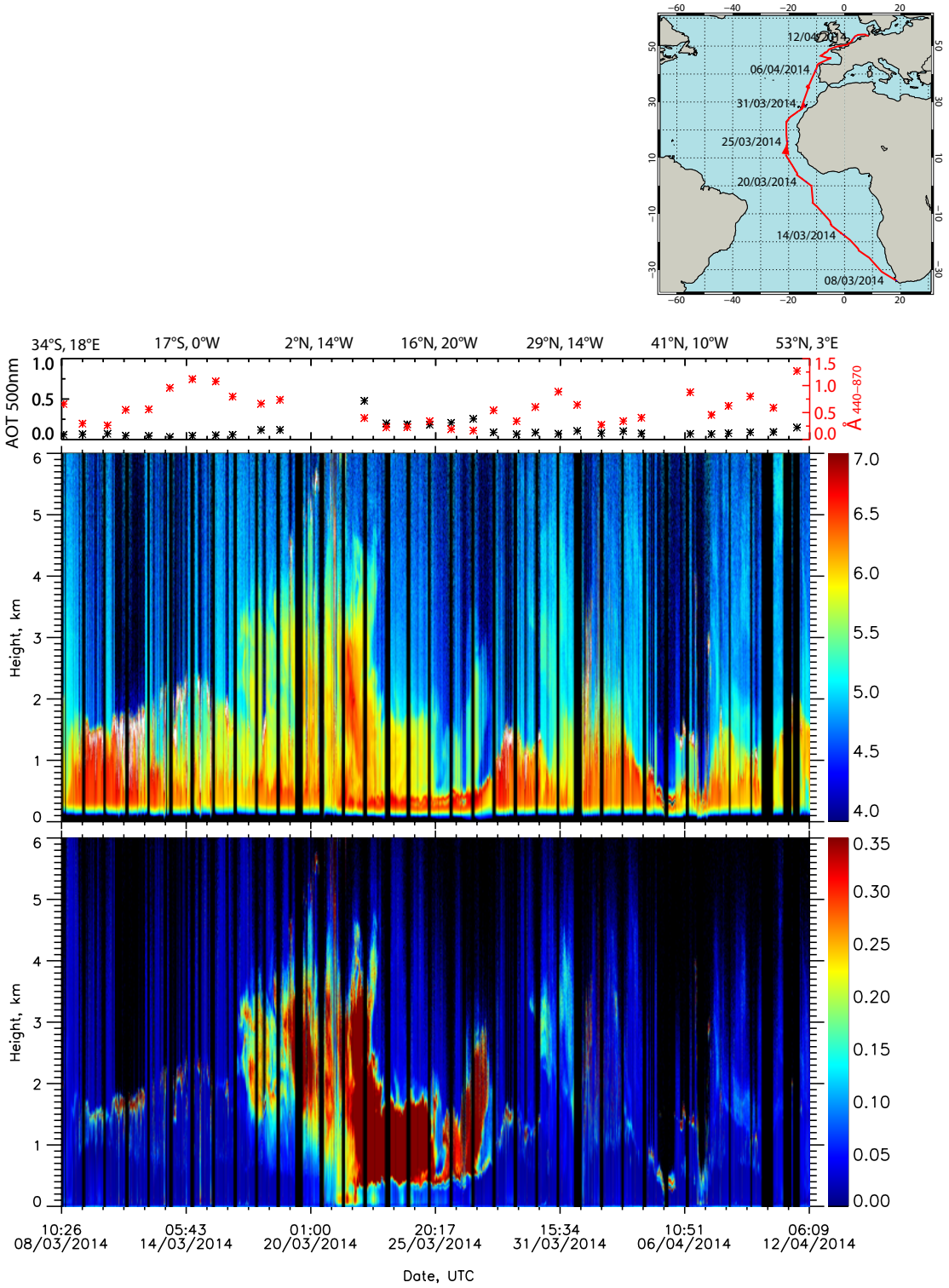


**Figure 4.7:** Same as Fig. 4.6 but for PS83. Additionally, the sun photometer derived 500 nm AOT and 440/870 nm backscatter-related Ångström exponent are shown.

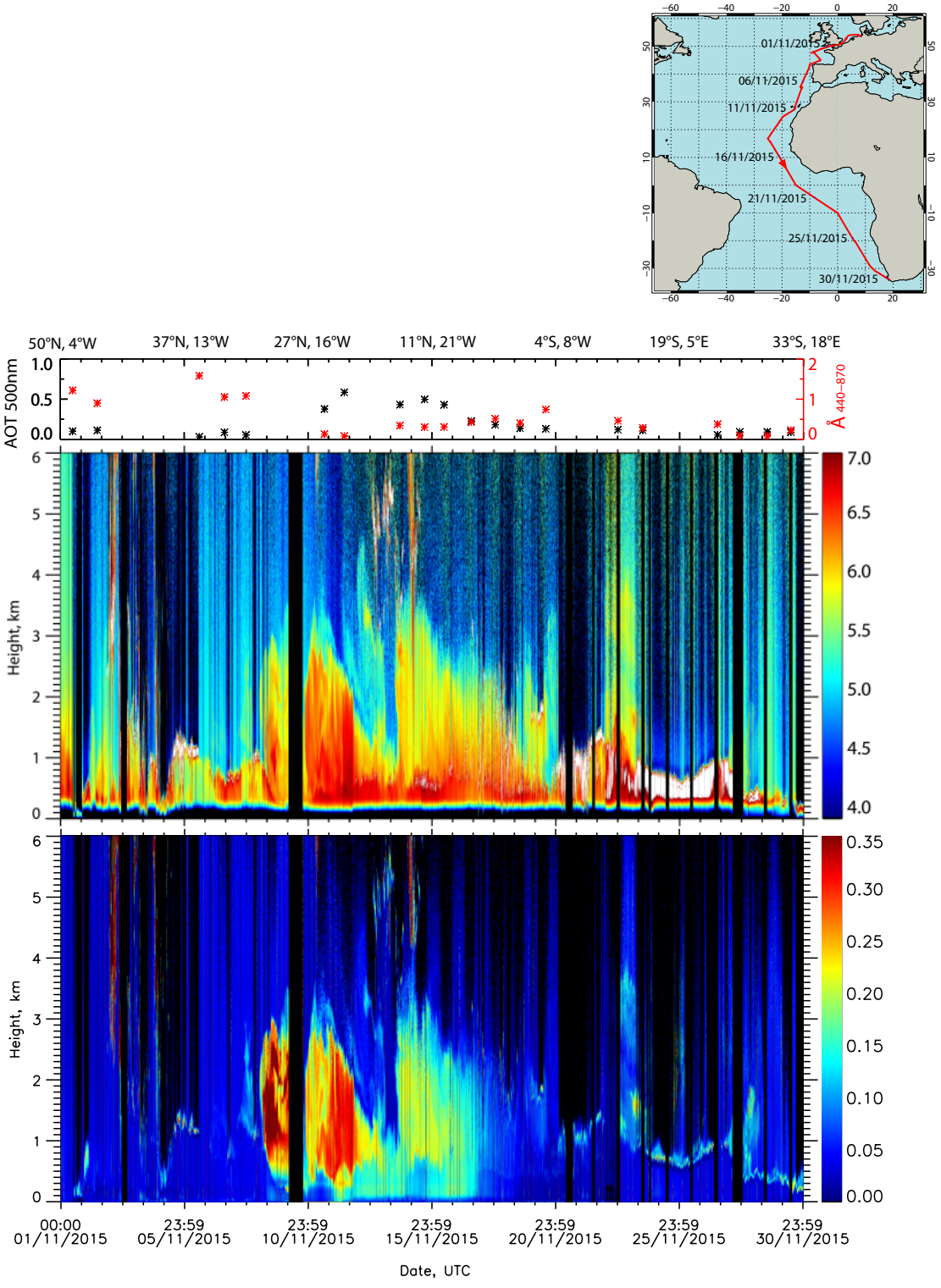


**Figure 4.8:** Same as Fig. 4.7 but for the autumn cruise PS95.

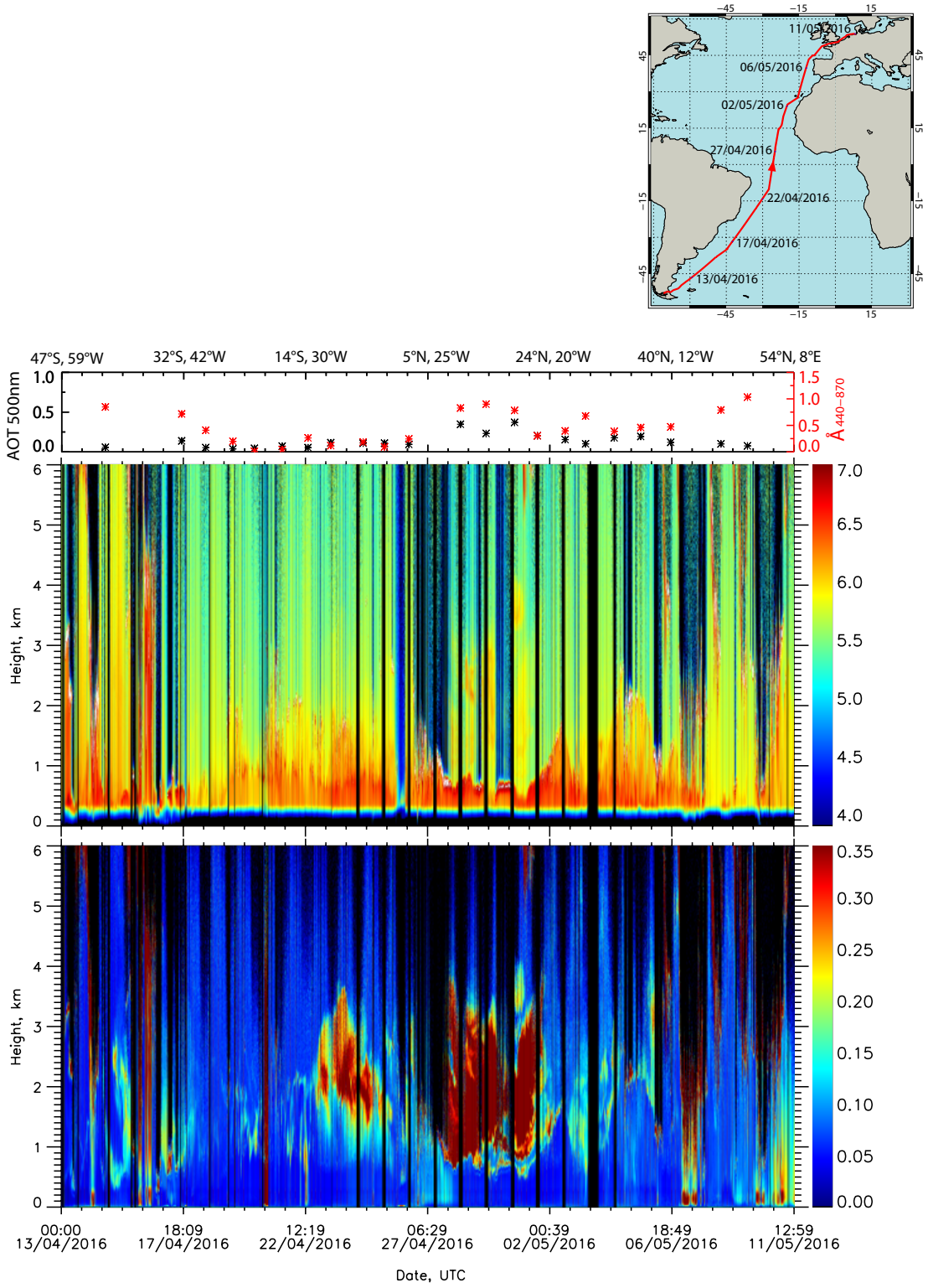


**Figure 4.9:** Same as Fig. 4.5 but for the spring cruise PS98.

# Chapter 5

# Results - Part I: Case studies

In this section case studies are analysed to investigate the aerosol above and in the MBL. The focus will be on the two recent cruises PS95 and PS98, because the setup of the used lidar system (near-range channels) enables profiles down to about 120 m and therefore information of the properties in the MBL. In the second part, a statistical analysis of all analysed measurements will provide an overview of latitudinal trends.

Three night measurements from PS95 and PS98 were selected to present a detailed discussion of the optical properties in the MBL and in lofted layers. On 30 November 2015, during the autumn cruise PS95, almost pure marine conditions could be observed and on 11 November 2015, Saharan dust was measured near the Canary Islands. During the spring cruise 2016 (PS98), Saharan dust and biomass-burning aerosol mixtures were detected near the Cape Verde Islands.
Profiles of the optical properties derived from the lidar measurements such as backscatter and extinction coefficient, lidar ratio, Ångström exponent and depolarisation ratio as well as profiles of temperature and relative humidity determined from GDAS1 data are presented for each case. To determine possible aerosol sources, backward trajectories, calculated with the HYSPLIT model, are discussed.

## 5.1 PS95 - Marine aerosol conditions

At the end of the cruise PS95 on 29 and 30 November 2015, marine conditions could be observed.
In Figure 5.1, the time series of the range-corrected signal at 1064 nm and the volume depolarisation ratio at 532 nm from 29 and 30 November 2015 are shown. Additionally, the AOT at 500 nm and the Ångström exponent at 440/870 nm retrieved by sun photometer measurements are shown in the upper panel. Mean AOT at 500 nm of 0.09±0.01 on 29 November (0.09±0.02 on 30 November) and an Ångström exponent of 0.08±0.02 (0.23±0.08) are in good agreement with previous MAN results for remote oceanic areas, not influenced by con-

tinental aerosol sources. In these regions, the AOT at 500 nm is typically below 0.1 and $Å \approx 0.6$ [*Smirnov et al.*, 2009].
In the time series of the volume depolarisation ratio, a thin depolarising layer at the top of the MBL, at 300–400 m, can be observed.
Mean profiles of the measured optical properties are shown in Fig. 5.2 for 30 November 01:15–02:30 UTC with a vertical smoothing length of 127.5 m. For extinction coefficient, lidar ratio and Ångström exponent profiles, a smoothing length of 127.5 m in the boundary layer and 457.5 m above 340 m height was used to reduce signal noise. Nevertheless, high signal noise

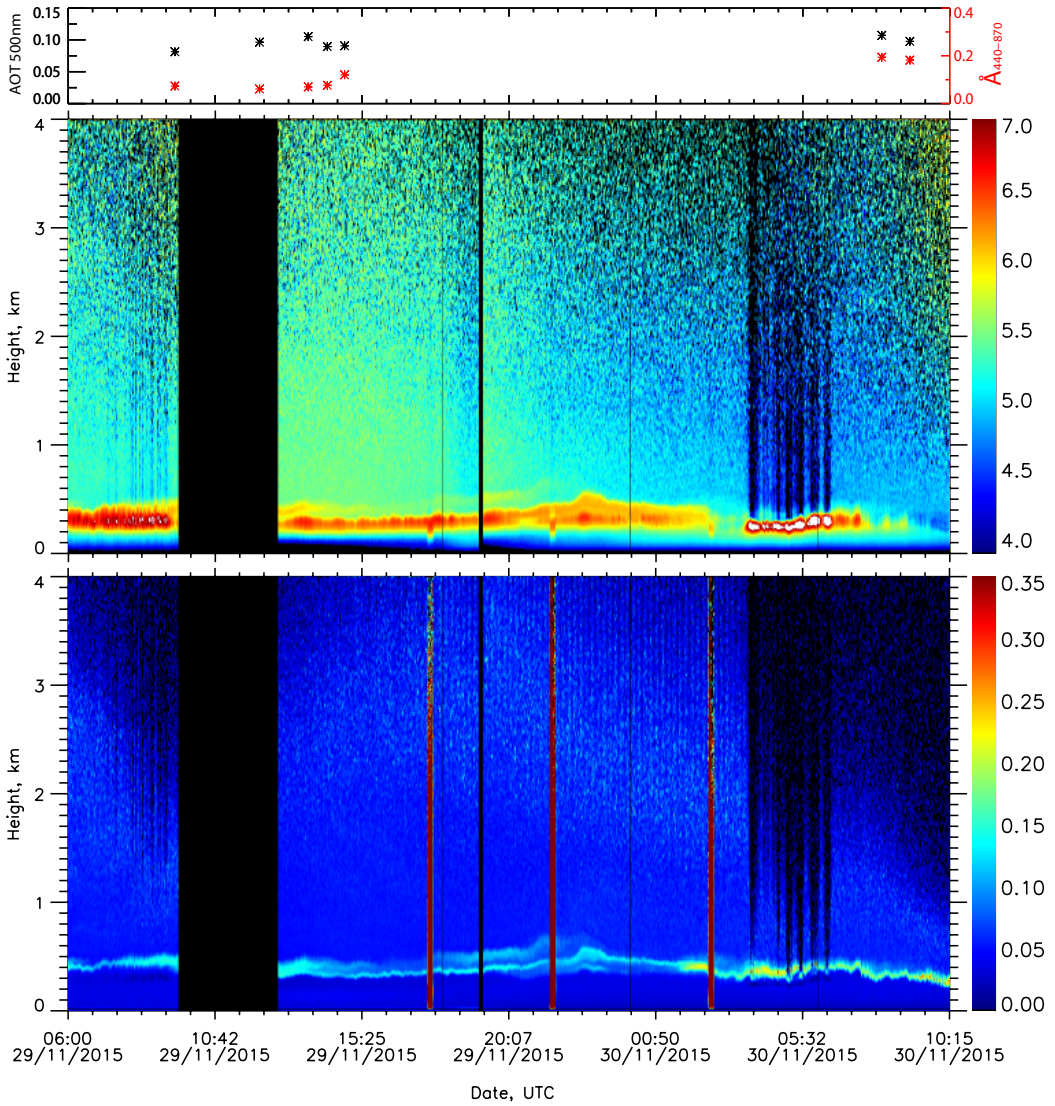


**Figure 5.1:** Marine conditions during PS95: time series of the Microtops sun photometer derived AOT at 500 nm and 440/870 nm Ångström exponent (upper panel), 1064 nm range-corrected signal (middle panel) and 532 nm volume depolarisation ratio (lower panel). Vertical red bars indicate depolarisation calibration measurements.

does occur in the extinction coefficient profile above 500 m due to the very low aerosol concentrations. Such noisy profiles will be cut off in the following examples as the lidar is not sensitive enough and correspondingly the signal-to-noise ratio is too low in regions of such low (almost zero) extinction coefficients. In the last panel, GDAS1 and radio sounding profiles are shown. GDAS1 data represent temperature and relative humidity profiles at 0 UTC, whereas the radio sounding profile represents atmospheric conditions at 12 UTC.
According to the backscatter coefficient and the GDAS1 and sounding profile in Fig. 5.2, the MBL top height was only about 300 m. Within the MBL, the lidar ratio was 23±2 sr at 355 nm and 23±1 sr at 532 nm, which agrees with results during ACE-2 ($S_{532}$ 23±3 sr,[*Müller et al.*, 2007]) and SAMUM-2a ($S_{532}$ 18±4 sr and $S_{355}$ 18±2 sr,[*Groß et al.*, 2011]).
The increase of the depolarisation ratios at the top of the MBL should be highlighted. Particle and volume depolarisation ratio at 355 nm and 532 nm are around zero in the MBL (large, non-depolarising particles) and increase from 300 m to about 400 m (volume depolarisation) and 450 m height (particle depolarisation) shortly above the MBL top. After this peak, the depolarisation decreases to about zero again. Considering the profiles of relative humidity and temperature, a correlation with the relative humidity is obvious. The relative humidity decreases from about 90% near the ground to under 20% above 600 m. Simultaneously the temperature increases. HYSPLIT backward trajectories (Fig. 5.3) indicate that the air parcels arriving at 300, 600 and 1000 m had only been carried over the South Atlantic Ocean the last 7 days, thus it can be assumed that the airmass contains mostly marine aerosol originated from the ocean, e.g. sea salt. Sea salt aerosol exists as dry particles at low relative humidity (RH). Since sea salt is hygroscopic, the salt particles absorb water to form droplets when the RH exceeds the deliquescence relative humidity (DRH). If the RH decreases to the crystallization relative humidity (CRH), the particle crystallize from the droplet. At a

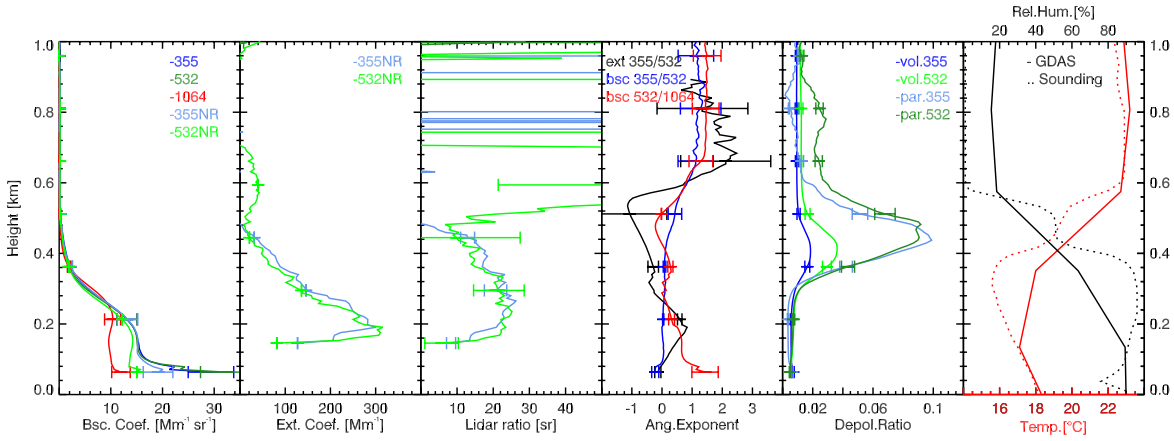


**Figure 5.2:** Profiles averaged for 30 November 2015, 01:15–02:30 UTC. Backscatter coefficient and depolarisation ratios smoothed with 127.5 m vertical length. Extinction coefficients, lidar ratios and Ångström exponents are smoothed with 127.5 m till 242 m and afterwards with 367.5 m. Meteorological data from GDAS1 (30 November 2015, 00 UTC) and radio sounding measurements (29 November 2015, 12 UTC) are also presented.

RH above the CRH, the sea salt particles are in solution with water and show low values of $\delta \approx 3\%$ [*Tesche et al.*, 2011a]. When the RH is below the CRH, the sea salt particles crystallise and exist as non-spherical particles due to the cubic shape of NaCl, the main constitute of sea salt aerosol [*Kokhanovsky*, 2008]. As non-spherical particles they cause higher depolarisation ratios. In this case, dried sea-salt particles caused depolarisation ratios up to 9% at 532 nm and 10% at 355 nm. Previous studies showed similar results. *Murayama et al.* [1999] measured high depolarisation ratios ($\approx 10\%$) at 532 nm in the lower atmosphere associated with sea breeze events in the coastal area of Tokyo Bay. *Sakai et al.* [2000] observed low depolarisation ratios (<5%) at 532 nm over a wide range of relative humidities, whereas $\delta^{par} > 10\%$ was measured at low RH (<50%) in air masses which had passed over the Pacific Ocean. In a laboratory chamber experiment *Sakai et al.* [2010] found linear depolarisation ratios at 532 nm of $1\pm \leq 0.1\%$ for droplets, $8\pm1\%$ for sea salt crystals and $21\pm2\%$ for NaCl crystals.

Thus we can conclude that marine particles were transported above the MBL top, dried and crystallised and therefore cause a high particle depolarisation ratio even though the backscattering is low compared to the MBL.

The extinction and backscatter-related Ångström exponents are low in the MBL and increase above the layer with higher depolarisation ratio. Since low $\mathring{A}$ is an indicator for large particles and higher $\mathring{A}$ indicates small particles, the particles above the mentioned layer are smaller than the particles below, which is in good agreement with the hypothesis of the dried marine aerosol layer above the MBL.

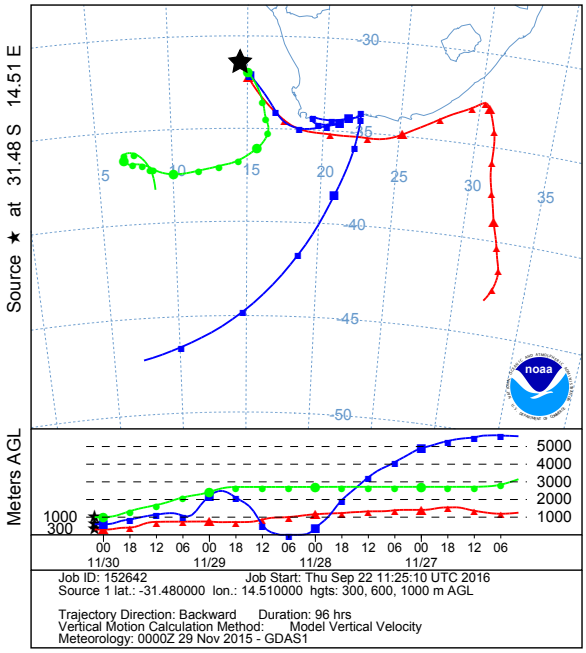


**Figure 5.3:** NOAA HYSPLIT backward trajectories for 4 days ending at the position of Polarstern (31.48°S, 14.51°E, marked by the black star) on 30 November 2015, 02:00 UTC at 300 m, 600 m and 1000 m AGL.

## 5.2 PS95 - Saharan dust

When Polarstern approached the Canary Islands during the autumn cruise 2015, the first dust plume was observed in the evening of 10 November at around 28°N. The dust could be measured until 14 November. Later another dust plume with a lower depolarisation ratio was observed (see Fig. 4.8).

Figure 5.4 (left) presents the column integrated concentration on 11 November 2015 12:00 UTC from the BSC-DREAM8b model (Dust REgional Atmospheric Model), operated by the Barcelona Supercomputing Center (`http://www.bsc.es/ESS/services/BSC-DREAM8b`, accessed: 14/11/1016). The increased column dust load above the Atlantic at the position of Polarstern is illustrated by the dark green colour. According to HYSPLIT backward trajectories (Fig. 5.4 right), the air mass measured on 11 November 20 UTC originated from the Saharan desert. Only air masses that arrived at 3 km had been carried also over European areas in the last 7 days.

The range-corrected signal at 1064 nm and the 532 nm volume depolarisation ratio of the first dust plume are shown in Fig. 5.5. Additionally, sun photometer measurements from 11 and 12 November are given. The sun photometer retrieved Ångström exponent at 440/870 nm is 0.13 on 11 November and 0.08 for the day after. The daily averaged AOT at 500 nm for these days is 0.38 (11 November) and 0.58 (12 November). The dust layer reached heights about 3 to 3.5 km on 11 November and slightly descended towards the 14 November. From

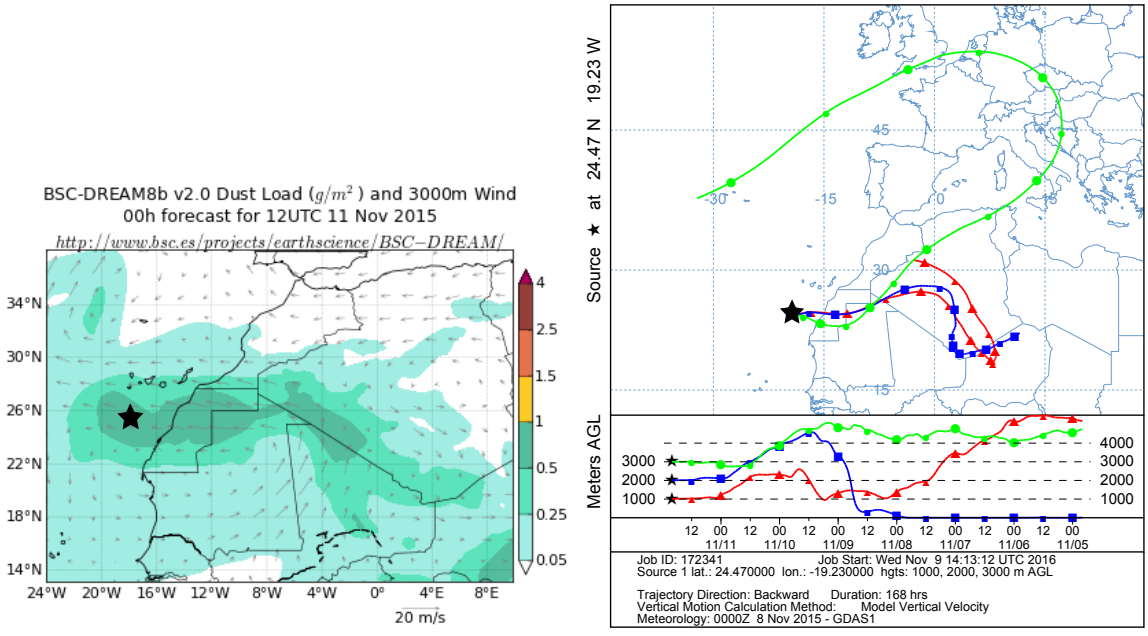


**Figure 5.4:** BSC DREAM Dust load for 11 November 2015, 12 UTC and 7-day NOAA HYSPLIT backward trajectories ending at the position of Polarstern on 11 November 2015, 20:00 UTC (24.27°N, 19.23°W). The position of Polarstern is marked by the black star.

13 November lofted layers between 2–3.5 km with a lower depolarisation ratio than the first dust plume could be observed at around 3 km.
Averaged profiles of the measured optical properties and the GDAS1 profiles of temperature and relative humidity are shown in Fig. 5.6 for 11 November 19:30–21:00 UTC (white frame Fig. 5.5). Backscatter coefficients and depolarisation ratios are smoothed with a vertical smoothing length of 187.5 m. Extinction coefficients, lidar ratios and Ångström exponents are smoothed with a vertical length of 367.5 m. The backscatter coefficient at 1064 nm is not considered reliable in the near range below 500 m because the applied Raman method assumes equal overlap functions of the elastic (here 1064 nm) and inelastic (607 nm) chan-

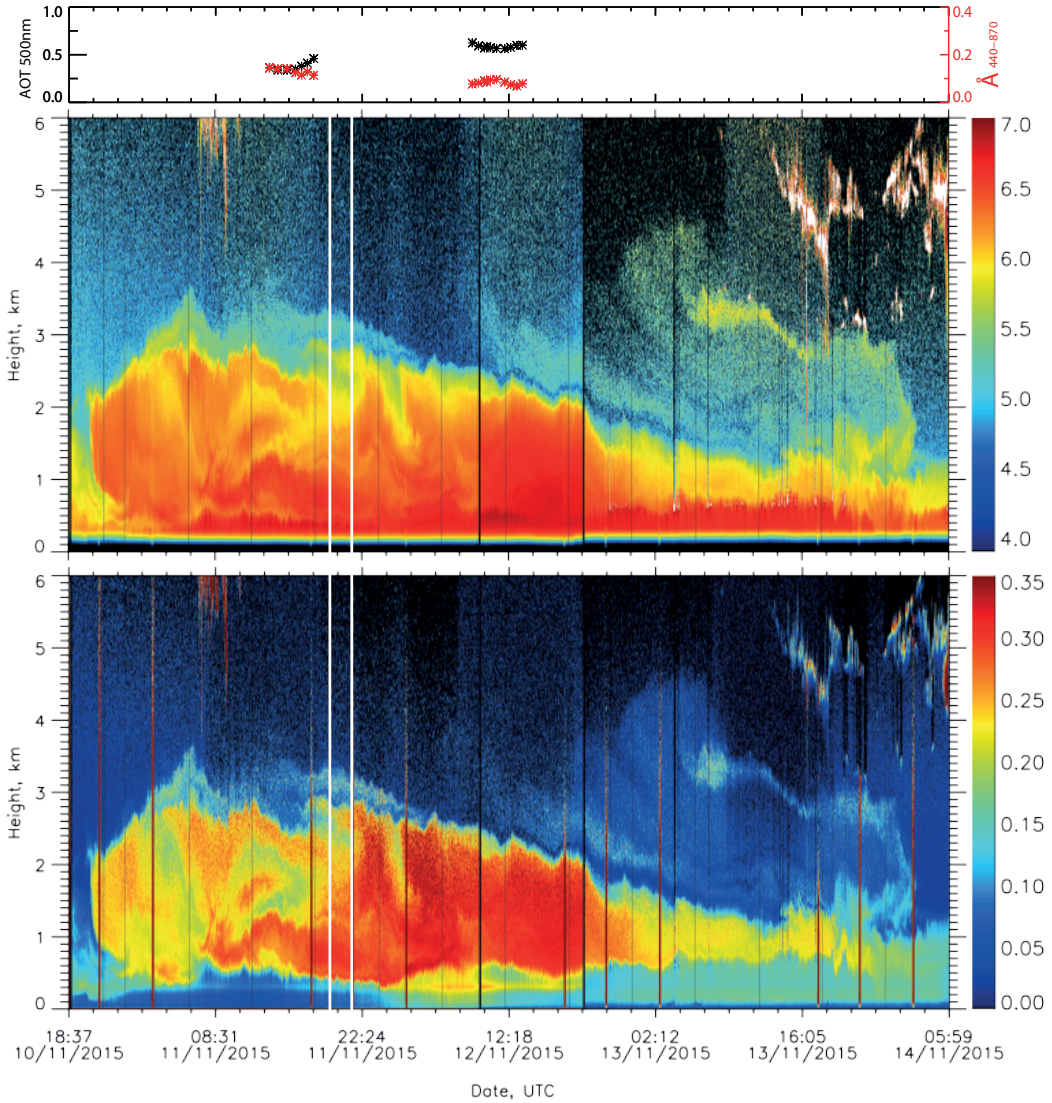


**Figure 5.5:** First dust event observed during PS95: time series of the Microtops sun photometer derived AOT (500 nm) and 440/870 nm Ångström exponent (upper panel), 1064 nm range-corrected signal (middle panel) and 532 nm volume depolarisation ratio (lower panel).

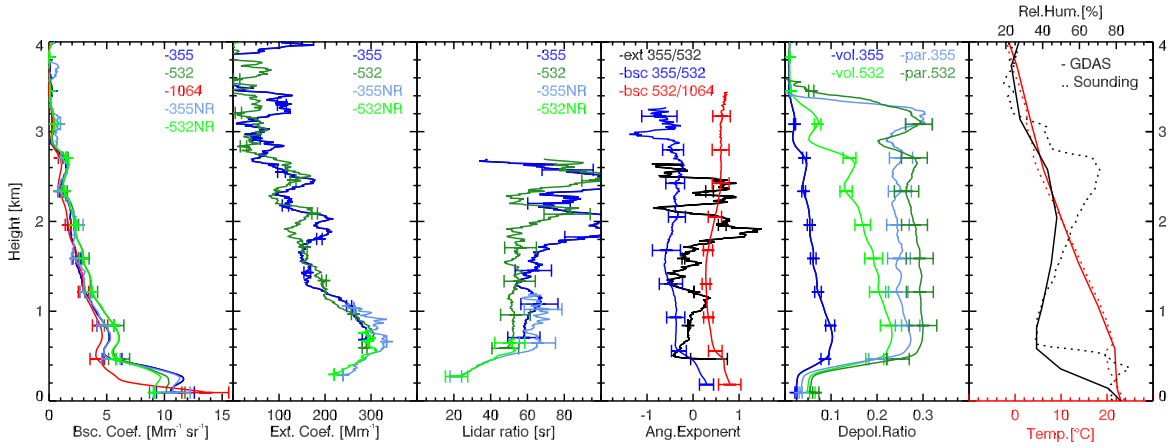


**Figure 5.6:** Profiles averaged for 11 November 2015, 19:30–21:00 UTC. Backscatter coefficient and depolarisation ratios smoothed with 127.5 m vertical length. Extinction coefficients, lidar ratios and Ångström exponents are smoothed with a vertical length of 367.5 m. Radio sounding profiles from 11 November 2015, 12 UTC and GDAS1 profiles (11 November 2015, 18 UTC) are presented in the right panel.

nel. As the used inelastic scattered light is not the corresponding Raman scattered light of 1064 nm but of 532 nm, this assumption is obviously not valid in the near-range of the lidar. The backscatter coefficient profiles show an increased backscatter coefficient at all wavelengths up to 2.8 km above the MBL (top height 400 m). The 532 nm backscatter coefficient is significantly larger than the 355 nm signal, whereas the extinction coefficient is wavelength independent. Even though, this is an untypical spectral behaviour, comparable observations of higher 532 nm than 355 nm backscatter coefficient were already observed in dust layers near the Cape Verde Islands [*Rittmeister*, 2015] and during the SHADOW campaign in Senegal [*Veselovskii et al.*, 2016]. The aerosol layer between 600 m and 2.8 km is characterised by a nearly height constant particle depolarisation ratio of 29±1% at 532 nm and 25±1% at 355 nm. The increased particle depolarisation ratios indicate a non-spherical particle shape and are in good agreement with values found for pure dust during SAMUM-2a ($\delta_{532}^{par} \approx 30\%$ and $\delta_{355}^{par} \approx 25\%$ [*Groß et al.*, 2011; *Tesche et al.*, 2011a]). The mean lidar ratio at 532 nm (355 nm) is 53±2 sr (61±4 sr) in the height of the lofted aerosol layer. The lidar ratio at 355 nm is larger than at 532 nm, which results from the higher backscatter coefficient at 532 nm and agrees with values found for dust during the SHADOW campaign [*Veselovskii et al.*, 2016]. The mean backscatter-related 355/532 nm Ångström exponent is $-0.4 \pm 0.1$. *Veselovskii et al.* [2016] explains these negative values as a result of the spectral dependence of the imaginary part of the dust refractive index, which is larger at 355 nm than at 532 nm (shown by *Müller et al.* [2009]). The extinction-related $\mathring{A}$ at 355/532 nm of 0.1±0.5 and the backscatter-related $\mathring{A}$ at 532/1064 nm of 0.4±0.1 are in good agreement with values for dust measured during SAMUM-2b ($\mathring{A}_{ext}^{355/532} \approx 0.22\pm0.27$, $\mathring{A}_{bsc}^{532/1064} \approx 0.45\pm0.16$ [*Tesche et al.*, 2011a]). Thus, the observed particles can be considered as pure dust.

The MBL reached a height of about 400 m according to the backscatter profile. Lidar ratios

at 532 nm and 355 nm are 30±3 sr and 30±2 sr in the MBL, which are higher than the characteristic values for marine aerosol (see marine case study Sec. 5.1) and suggest a mixture of marine aerosol with other particles. The particle depolarisation ratios are also slightly higher, 9% at 532 nm and 6% at 355 nm, and indicate the mixing of dust into the MBL.

## 5.3 PS98 - Mixed aerosol layers

During the spring cruise PS98, extended depolarising aerosol layers were observed near the Cape Verde Islands. The range-corrected signal and volume depolarisation ratio at 532 nm as well as Microtops sun photometer measurements on 29 April 2016 are shown in Fig. 5.7. Sun photometer measurements determined an average AOT at 500 nm of 0.23 and an Ångström-Exponent of 0.9 for 440/870 nm.
Mean profiles of the optical properties averaged from 29 April 2016 between 20:15–21:00 UTC are shown in Fig. 5.8. Backscatter coefficients and depolarisation ratios are smoothed with a vertical smoothing length of 187.5 m. For the calculation of extinction coefficient, lidar ratio and Ångström-Exponent a smoothing length of 457.5 m was used. The 532 nm near-range extinction coefficient and lidar ratio were left out because of a misalignment of the 532 nm near-range channel which do not affect the Raman backscatter retrievals.
An increased backscatter coefficient at both wavelengths indicates aerosol layers between 0.9–3 km. These layers are separated from the MBL, which reached a height of about 500 m according to the increased backscatter signal and GDAS1/radio sounding data.
The mean lidar ratio at 355 nm is 22±1 sr, the mean backscatter-related 355/532 Ångström exponent amount 0.9±0.0 and the mean particle depolarisation ratios are around zero at both wavelengths in the MBL. These values are indicators of a pure marine boundary layer without dust (see marine case, Sec. 5.1).
Regarding the backscatter profile, the aerosol-laden region above the MBL can be divided into four layers. The first layer extends from 0.9–1.2 km, the second layer from 1.3–1.6 km, the third from 1.7–2.5 km and the fourth layer extends from 2.6–3.0 km.
The mean lidar ratio in the first layer is 48±4 sr and 46±9 sr at 532 nm and 355 nm, respectively. The mean backscatter-related 355/532 Ångström exponent is 0.4±0.1 and range between the typical values of dust (0.16±0.45, SAMUM-2b) and smoke (0.90±0.26, SAMUM-2a [*Tesche et al.*, 2011b]). Same applies for the mean particle depolarisation ratio, which is 20±2% at 532 nm and 15±2% at 355 nm. These values are in good agreement with values for dust and smoke mixtures measured during SAMUM-2a ($\delta^{par}_{355,532} \approx 16\%$, [*Tesche et al.*, 2011a]).
The second layer extends from 1.3–1.6 km. The mean lidar ratio is 57±7 sr and 63±8 sr at 532 nm and 355 nm, respectively. Mean backscatter and extinction-related $\AA$ at 355/532 nm amount 0.1±0.1 and 0.4±0.2, respectively. The mean particle depolarisation ratio of 24±2% at 532 nm and 19±2% at 355 nm suggest a mixture of depolarising dust ($\delta^{par}_{532} \approx 31\%$ [*Tesche et al.*, 2011a]) and non-depolarising smoke ($\delta^{par}_{532} \approx 5\%$ [*Tesche et al.*, 2011a]). The fraction of dust and smoke can be estimated using a method described by *Tesche et al.* [2009a].

Assuming a $\delta_{532}^{par}$ of 31% for pure dust and 5% for smoke, the fraction of dust in this layer amount around 77%.
In the third and fourth layer the extinction coefficient and therefore the lidar ratio show a significant wavelength dependence. The extinction at 355 nm is higher than at 532 nm. Lidar ratio and backscatter-related Ångström exponent in the third layer are comparable with values in the first layer. The mean lidar ratio at 532 nm amount 40±4 sr and 47±9 sr at 355 nm. The mean backscatter and extinction-related $\AA$ at 355/532 nm is 0.4±0.1 and 0.7±0.7, respectively. Whereas lidar ratio and Ångström exponents remain nearly constant in this layer, the particle depolarisation ratio ($\delta_{532}^{par} \approx 19\%$) is significant higher at the top

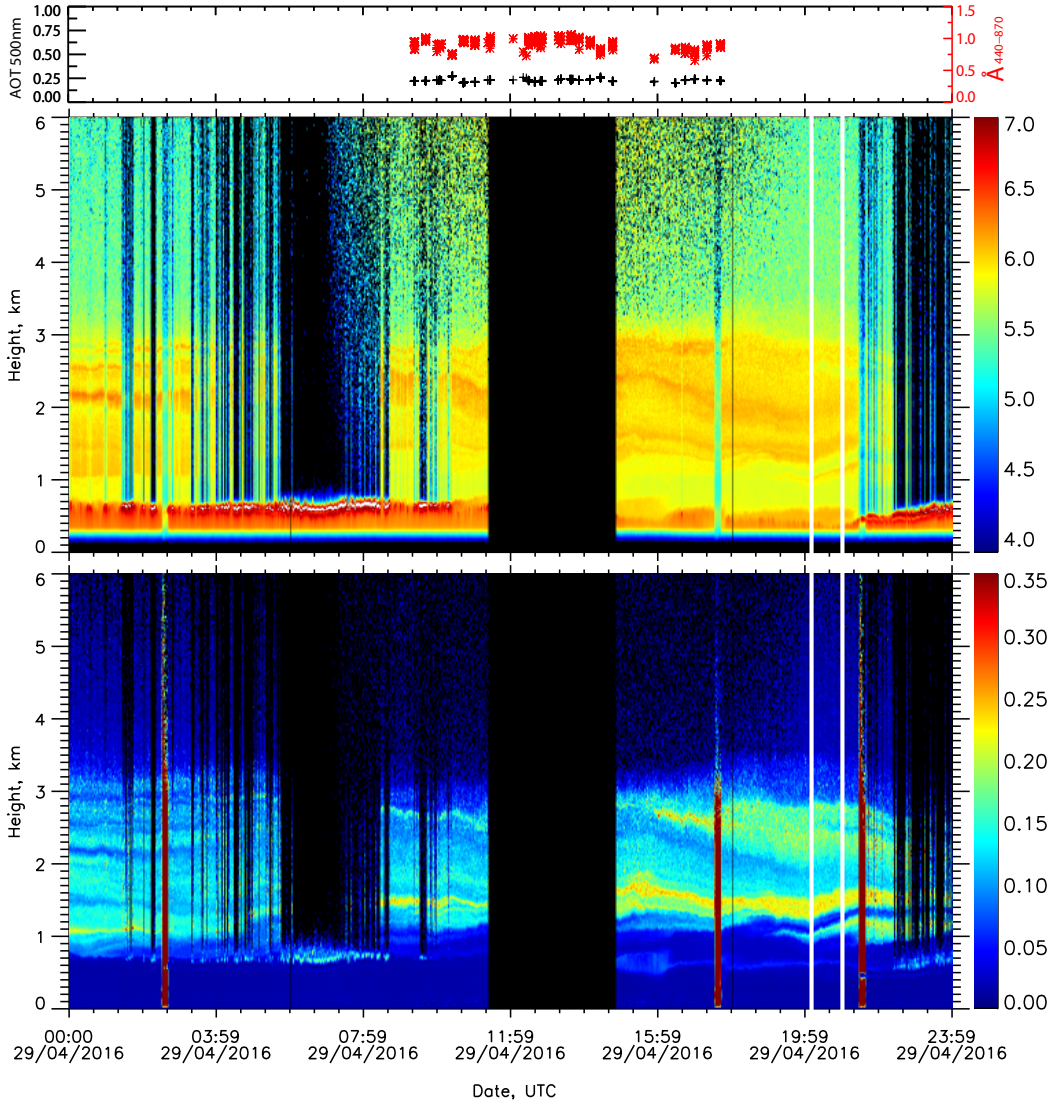


**Figure 5.7:** Complex aerosol layering with smoke and dust on PS98: Sun photometer derived AOT at 500 nm and 440/870 nm Ångström exponent (upper panel), 532 nm range-corrected signal (middle panel) and volume depolarisation ratio (lower panel).

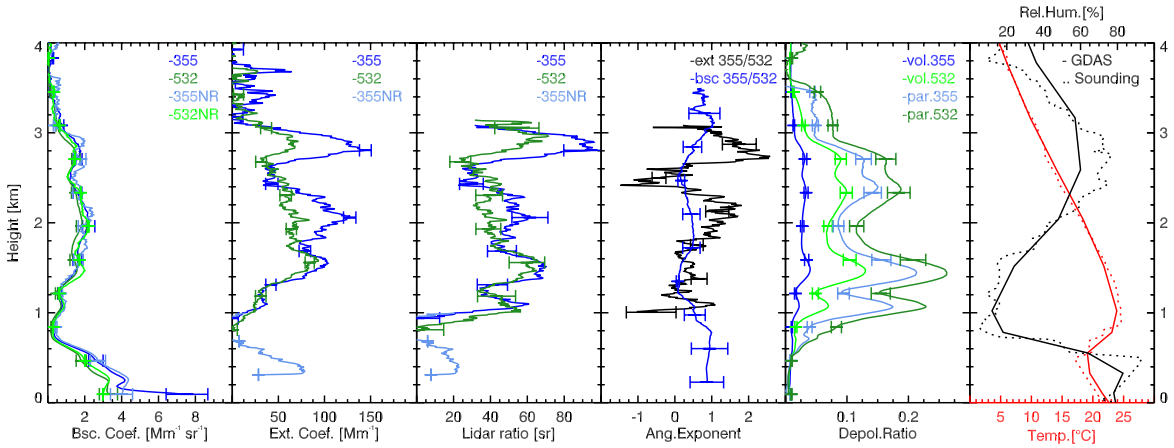


**Figure 5.8:** Averaged profiles for 29 April 2016, 20:15–21:00 UTC. Meteorological data from GDAS1 (29 April 2016, 21 UTC) and radio sounding measurements (29 April 2016, 15 UTC).

than at the base ($\delta_{532}^{par} \approx 11\%$). This may result from different aerosol sources, alterations during transport or mixing processes.

The fourth layer is characterised by a high lidar ratio of 88±8 sr at 532 nm and 60±6 sr at 355 nm and high backscatter and extinction-related Ångström exponents of 0.6±0.1 and 1.6±0.3, respectively, which indicate the presence of large, absorbing particles. Mean particle depolarisation ratios of 13±3% and 9±3% at 532 nm and 355 nm also indicate an amount of depolarising particles. Using the dust-smoke separation method described by *Tesche et al.* [2009a], the fraction of dust amount around 36%. The fraction of smoke is therefore significantly higher than in the other layers.

Figure 5.9 presents the HYSPLIT backward trajectories for the last 10 days arriving at the position of Polarstern at different altitudes. Air masses arriving in the MBL (500 m) had been carried only over the Atlantic Ocean the last 10 days and therefore contained mostly marine aerosol. Air masses arriving between 1–3 km were advected from the African continent. The air masses arriving at 1 km height originated from the Saharan desert and passed over active fire areas south west of the Saharan desert 6 days before arriving at the position of Polarstern. Trajectories arriving at 1.5 km and 2 km also passed over the Saharan desert and active biomass-burning regions, but have never been close to the ground. As investigated by *Nisantzi et al.* [2014], fires can support the upward transport of dust into the free troposphere. A high amount of dust besides biomass-burning aerosol could therefore also be detected in these altitudes. In contrast, air masses arriving at 2.5 km and 3 km were on ground level over active fire regions for several days and could take up a high amount of biomass-burning aerosol.

Summing up, one can state that during this night measurement, four layers with different fractions of dust and smoke could be detected. At the same time, the MBL was almost pure marine without mixed-in dust or smoke particles. This case study shows the impact of different particle sources and trajectories on the aerosol occurrence over the ocean.

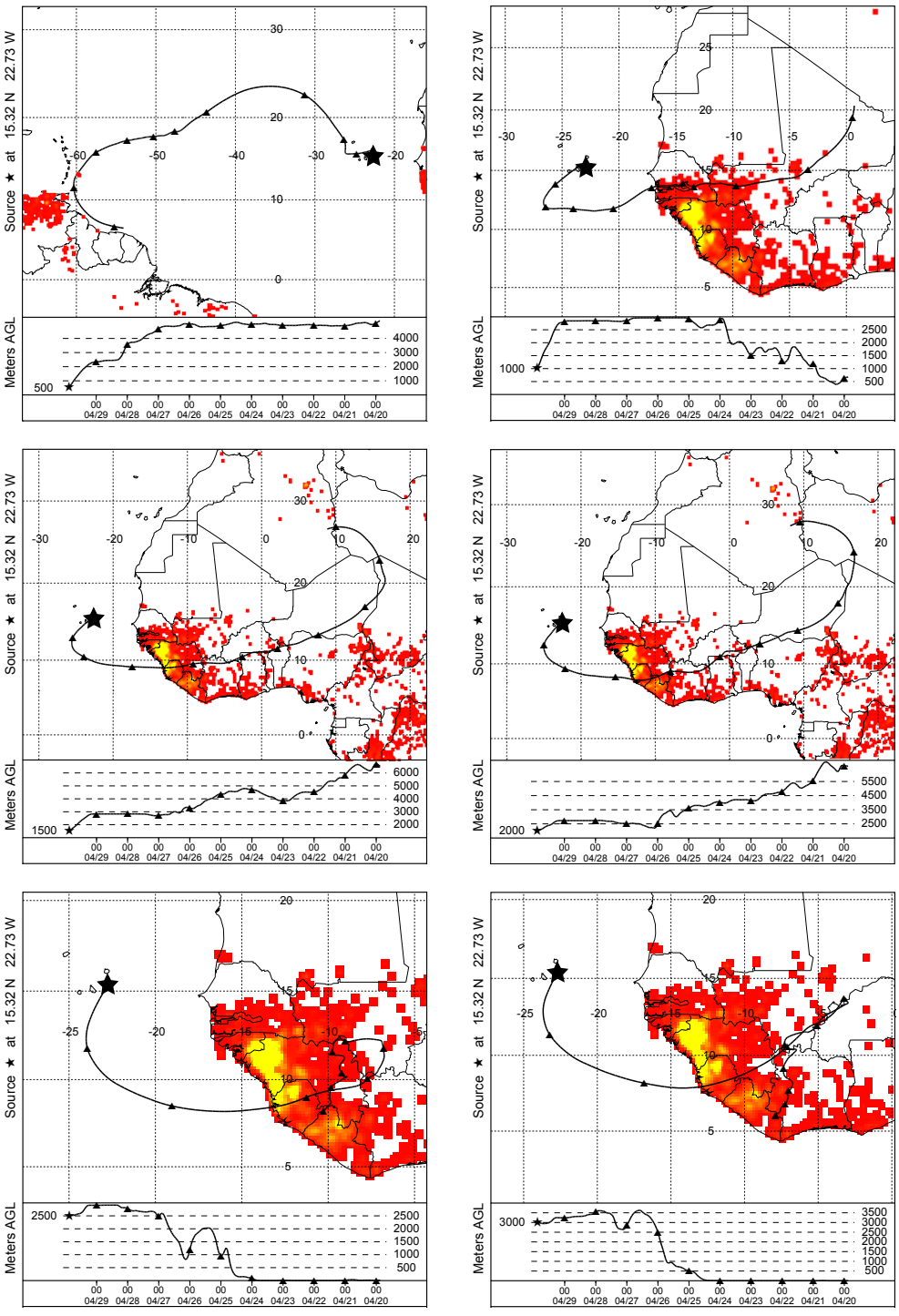


**Figure 5.9:** NOAA HYSPLIT backward trajectories ending at 29 April 2016 21:00 UTC at the position of Polarstern (15.32°N, 22.73°W, marked by the black star) at different altitudes. Additionally, fires detected by MODIS on board the Terra and Aqua satellites are shown. Fires are accumulated over the 10-day period from 20 April 2016 to 29 April 2016. Yellow color indicates a large number of fires, red dots indicate a low number of fires in the considered period (https://lance.modaps.eosdis.nasa.gov/firemaps, accessed: 24/02/2017).

# Chapter 6

# Results - Part II: Statistical analysis

## 6.1 Time series

A total of 45 night measurements from PS95 and PS98 were selected for analysis with respect to optical aerosol properties using the Raman method. Each measurement was divided into specific layers. The MBL and, when present, elevated aerosol layers and layers above the marine boundary layer, which showed an increased depolarisation ratio as seen in the marine case study (Sec. 5.1) have been separately analysed. These layers directly above the MBL are named dried marine layers from now on. The MBL top height and the extent of the analysed elevated aerosol layers and dried marine layers are shown in Fig. 6.1 for the PS95 (upper panel) and PS98 (lower panel) cruise, illustrated with blue dots and black and red bars, respectively. The MBL top height ranges between 300 m and 900 m and shows no significant latitudinal trend.
Mean values of backscatter and extinction coefficient, lidar ratio and particle depolarisation ratio at 355 nm and 532 nm and the backscatter and extinction-related Ångström exponents are shown in Fig. 6.2–6.7. Blue dots illustrate the MBL mean values derived from near-range measurements. Mean values of the elevated aerosol layers are derived from far-range signals and are illustrated with black dots, whereas mean values of the dried marine layers are illustrated red. These mean values are derived from near range signals. An exception is the measurement from 20 April 2016 where the far-range signal is used because of the height of the dried marine layer. Error bars represent the standard deviation. Deviations from values determined previously in the case studies result from different smoothing lengths used during analysis. Measured signals are smoothed with a vertical smoothing length of 187.5 m for MBL and dried marine layers and 367.5 m for elevated aerosol layers.

### PS95

For 27 measurements from 1 November to 30 November 2015, the weather conditions and the instrument status allowed the analysis of the aerosol conditions over the Atlantic Ocean during PS95. Mean backscatter and extinction coefficient at 355 nm and 532 nm are shown

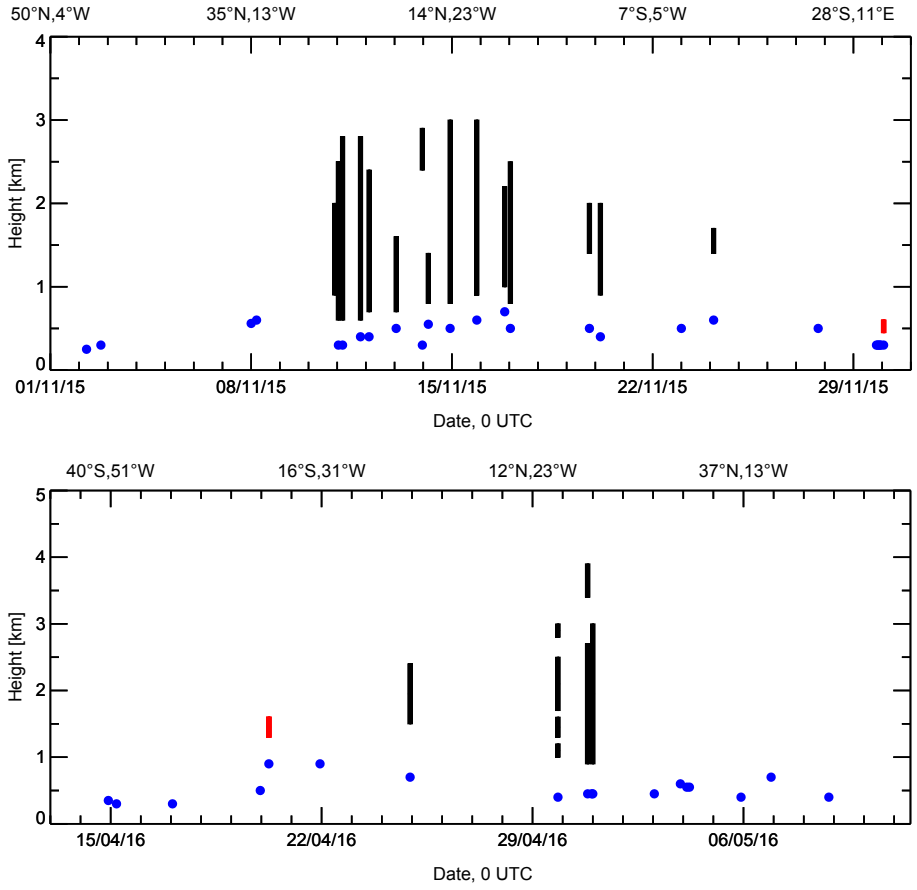


**Figure 6.1:** MBL top height (blue) and extent of the analysed elevated aerosol layers (black) and the dried marine layers (red) on PS95 (top panel) and PS98 (lower panel). Coordinates at the top mark the position of Polarstern at this time.

in Fig. 6.2. The mean MBL backscatter coefficients range from 2.8–10 $Mm^{-1}sr^{-1}$, whereas the backscatter coefficient in the elevated layers is lower and ranges between 0.6–5 $Mm^{-1}sr^{-1}$. Mean extinction coefficients range between 50–327 $Mm^{-1}$ at 355 nm and 38–323 $Mm^{-1}$ at 532 nm in the elevated layers and 65–318 $Mm^{-1}$ at 355 nm and 46–310 $Mm^{-1}$ at 532 nm in the MBL. Mean backscatter and extinction coefficients of dried marine layers are only shown for 30 November 01:15–02:30 UTC, because of a low signal-to-noise ratio in the height of these layers in the other observed cases.

An overview of the mean lidar and depolarisation ratios in MBL, elevated layers and dried marine layers is given in Fig. 6.3. Mean MBL lidar ratios are around 25 sr in the northern latitudes and 20 sr in the southern hemisphere at both wavelengths. In the region of dust, between 35°N and the equator, the mean lidar ratio in the MBL is around 30 sr. The increased lidar ratio is caused by downmixing of dust from higher altitudes, whereas the lidar ratio in the southern latitudes correlates with typical marine values (≈20 sr, [*Groß et al.*, 2011]). Anthropogenic aerosol from the European continent influence the MBL in northern

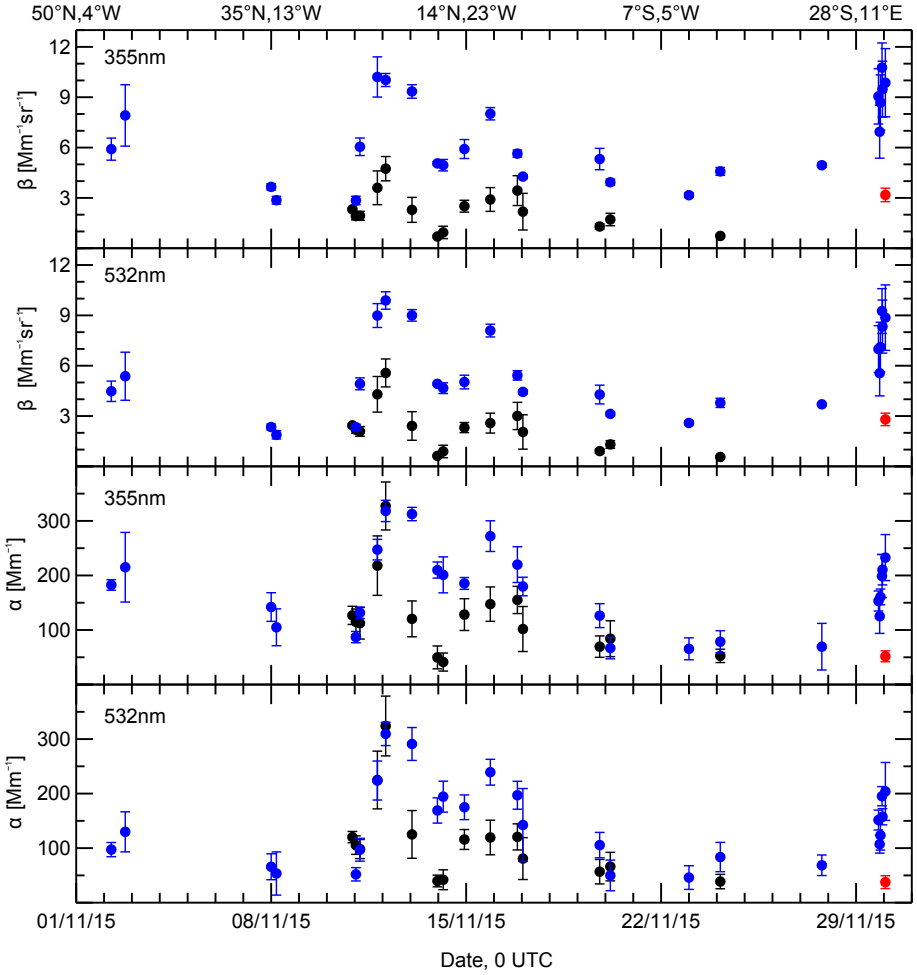


**Figure 6.2:** Mean values of the backscatter coefficient at 355 nm and 532 nm (upper two panels) and the extinction coefficient at 355 nm and 532 nm (lower two panels) for the analysed MBL (blue), elevated aerosol layers (black) and dried marine layers (red) on PS95. Error bars indicate the standard deviation.

latitudes, the lidar ratio therefore differs from typical marine values. The lidar ratio in the dried marine layer is slightly lower than the lidar ratio in the MBL the same day. Elevated layers are showing a mean lidar ratio between 44–70 sr (355 nm) and 41–67 sr (532 nm) which is in good agreement with typical values of dust and smoke and dust mixtures [*Tesche et al.*, 2011a]. On 13, 19 and 24 November, the lidar ratio is slightly higher than the other days while the particle depolarisation is significantly lower, which indicates a mixture with other absorbing, non-depolarising particles like biomass-burning aerosol.

The mean particle depolarisation ratio in the MBL is lower than 1% in the European influenced Atlantic and the southern hemisphere and show a strong increase in the Saharan influenced region between 35°N and the equator where values of about 18% are reached. The layer mean particle depolarisation is around 30% at the beginning of the dust plume

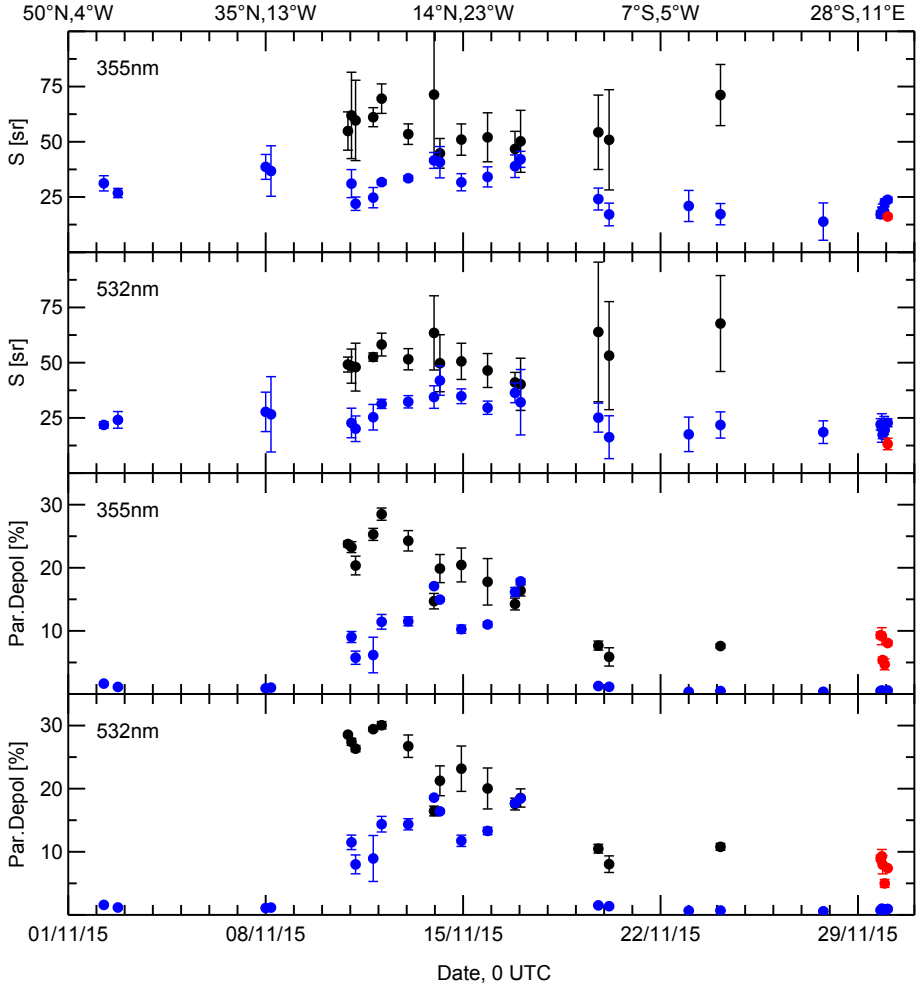


**Figure 6.3:** Mean values of the lidar ratio at 355 nm and 532 nm (upper two panels) and the particle depolarisation ratio at 355 nm and 532 nm (lower two panels) for the the analysed MBL (blue), elevated aerosol layers (black) and dried marine layers (red) on the PS95 cruise. Error bars indicate the standard deviation.

on 11 November 2015 and decreases towards the end, which suggests an increasing mixing with other less depolarising particles. The particle depolarisation ratios of all observed dried marine layers range between 4–9%.

Mean backscatter and extinction-related Ångström exponents are shown in Fig. 6.4. They range between 0 and 2 in the MBL as well as in the elevated layers. A latitudinal difference can be seen in the mean backscatter-related 355/532 nm Ångström exponent of the MBL. The mean $\mathring{A}_{bsc}^{355/532}$ is around 0 in the dust region whereas it is around 1 in the northern and 0.5 in southern latitudes. It can be concluded that there is a mixture of marine aerosol and large dust particles in the MBL between 35°N and the equator whereas in northern and southern latitudes the fraction of smaller particles in the measured marine boundary layers is higher. The mean $\mathring{A}_{bsc}^{355/532}$ in the elevated layers ranges between -0.5 and 0.5 in the

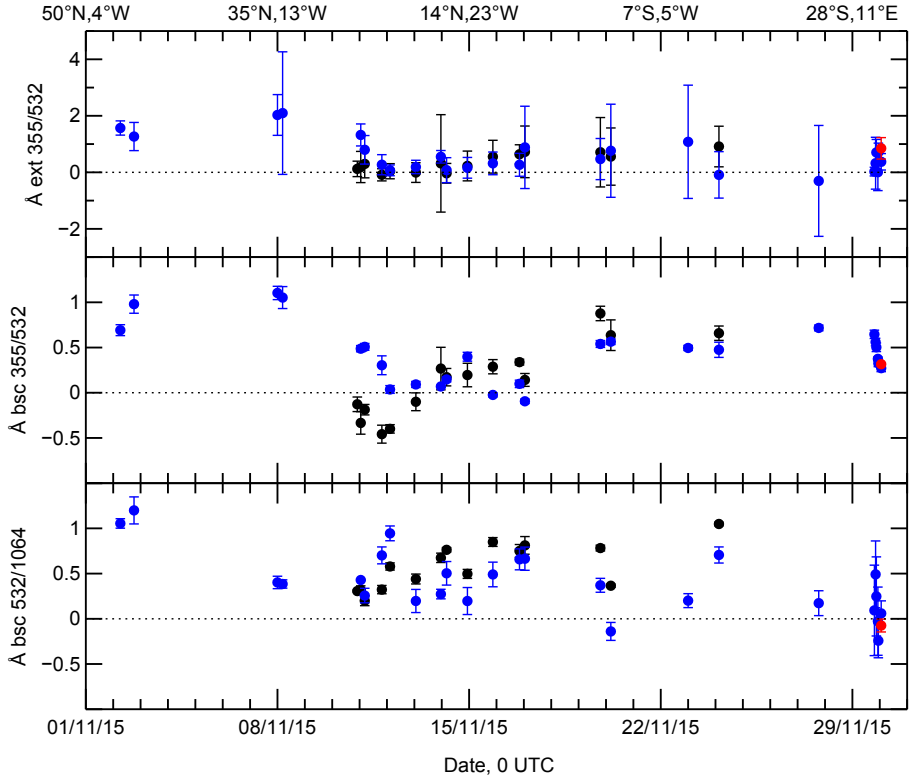


**Figure 6.4:** Mean values of the extinction-related Ångström exponent (upper panel) at 355/532 nm and the backscatter-related Ångström exponent at 355/532 nm (middle panel) and at 532/1064 nm (lower panel) of the analysed MBL (blue), elevated aerosol layers (black) and dried marine layers (red) on PS95. Error bars indicate the standard deviation.

region of the dust plumes. A difference between the first and second dust plume is obvious. From 11 to 14 November, $\mathring{A}_{bsc}^{355/532}$ is negative whereas it became positive during the second plume. According to *Veselovskii et al.* [2016] a low $\mathring{A}_{bsc}$ indicates an increased imaginary part of the refractive index at 355 nm compared to 532 nm and therefore a higher absorption at 355 nm than at 532 nm. This should be a result from different dust sources and particle properties. The backscatter and extinction-related Ångström exponent of the dried marine layer measured on 30 November are approximately similar to mean values of the MBL. The mean $\mathring{A}_{bsc}^{532/1064}$ in MBL and elevated layers does not show significant latitudinal differences.

## PS98

The second analysed cruise PS98 provides 18 MBL measurements and eight elevated dust layers including the layers characterised in the third case study. Additionally, one dried marine layer was observed on 20 April 2016. An overview of the analysed layers is given in the lower panel of Fig. 6.1.

Mean MBL backscatter coefficients (shown in Fig. 6.5) range between 2–9 $Mm^{-1}sr^{-1}$ at 355 nm and 1.6–6.5 $Mm^{-1}sr^{-1}$ at 532 nm. In the elevated layers, the mean backscatter

coefficient is significantly lower, 0.5–2.8 $Mm^{-1}sr^{-1}$ at 355 nm and 0.4–1.7 $Mm^{-1}sr^{-1}$ at 532 nm. The backscatter coefficient in the dried marine layer is comparable with those in elevated dust layers.

The mean extinction coefficients in the MBL range between 30–210 $Mm^{-1}sr^{-1}$ at 355 nm and 30–180 $Mm^{-1}$ at 532 nm. Again, the mean extinction coefficient in the dried marine layer is lower than in the MBL and in the same order of magnitude as elevated aerosol layers. Mean values in the MBL are higher in northern latitudes than in southern latitudes, which can be explained with a higher aerosol load in the continental influenced northern hemisphere.

Mean lidar ratio and particle depolarisation ratio are given in Fig. 6.6. Mean lidar ratios in the MBL range between 13 sr and 40 sr at both wavelengths. In contrast to PS95, there is no significant increase of the MBL lidar ratio in the dust region, between 10°S and 25°N. The mixing of dust into the MBL is therefore considered to be low. This is confirmed by a continuous low particle depolarisation ratio of less than 1% at both wavelengths in the MBL throughout the whole cruise. Elevated aerosol layers could be analysed between 10°S

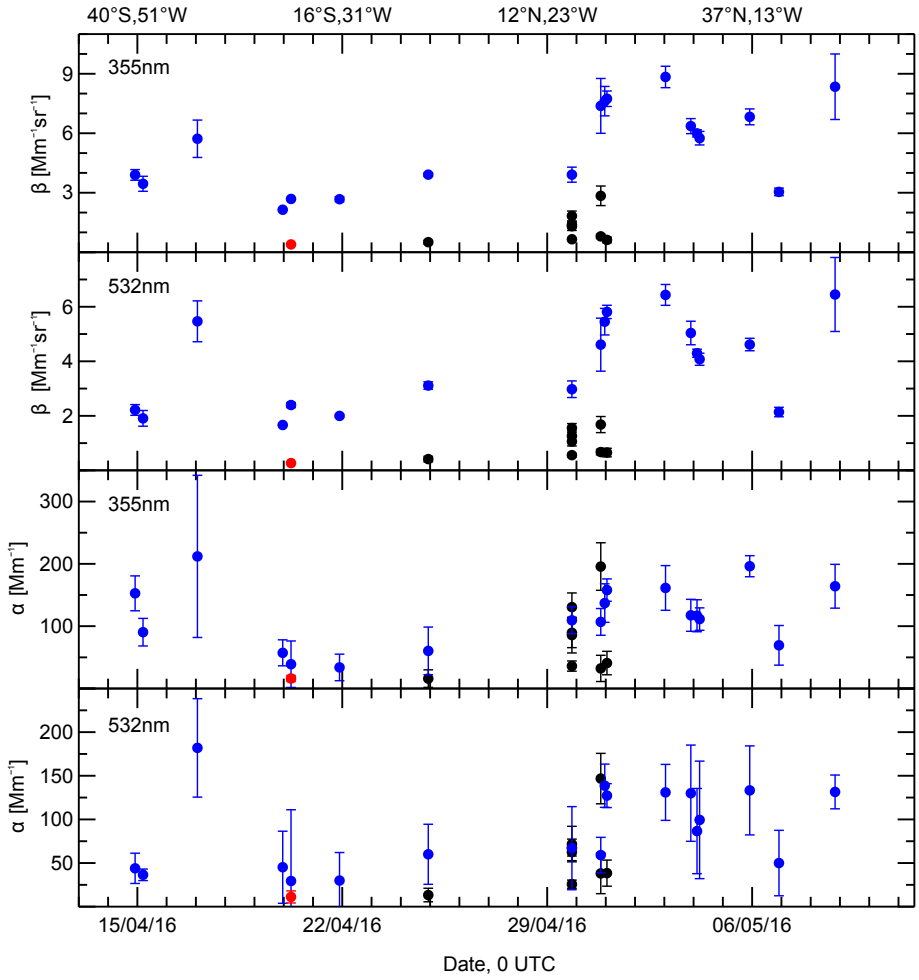


**Figure 6.5:** Same as Fig. 6.2 but for PS98 for the layers shown in Fig. 6.1.

and 25°N and show a wide range of mean lidar and particle depolarisation ratios, caused by different aerosol particle types in these layers. On 24 April, the lidar ratio is at both wavelengths around 35 sr considerable lower than characteristic values of pure dust ($S_{532} \approx$ 55 sr [*Tesche et al.*, 2011a]). This may result from marine aerosol transported upward by turbulent mixing processes. The upper aerosol layers on 29 and 30 April show a high lidar ratio (94 sr and 73 sr at 355 nm and 65 sr and 88 sr at 532 nm). At the same time, the depolarisation ratio is low (8% and 3% at 355 nm and 11% and 4% at 532 nm) indicating a high fraction of non-depolarising, highly absorbing aerosol like soot. Mean lidar ratios in the other analysed elevated layers range between 48–66 sr at 355 nm and 40–60 sr at 532 nm. Mean particle depolarisation ratio ranges between 11–22% and 15–26% at 355 nm and 532 nm, respectively. These values are lower than the characteristic values for pure dust and agree with values determined by *Groß et al.* [2011] during SAMUM-2 for dust and biomass-burning aerosol mixtures ($\delta^{par}$= 12–23% at both wavelengths). The dried marine

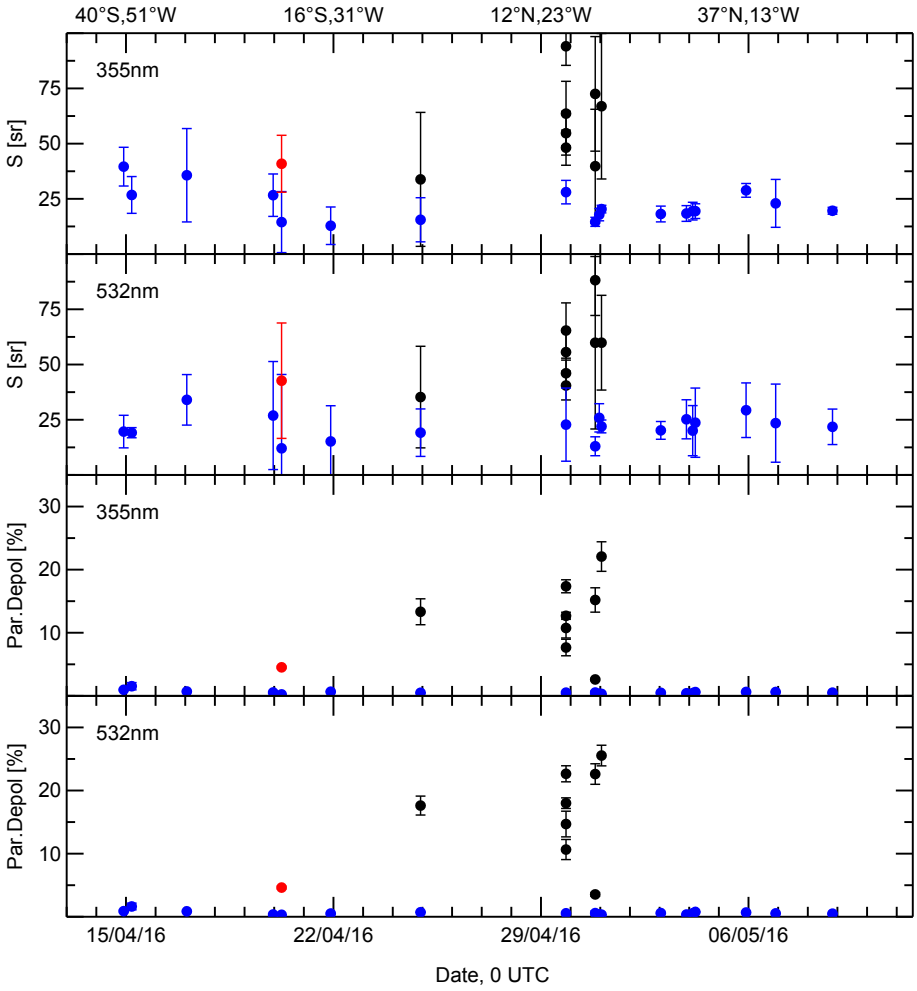


**Figure 6.6:** Same as Fig. 6.3 but for PS98.

layer on this cruise shows a lidar ratio around 40 sr and particle depolarisation of 5% at both wavelengths.
Extinction and backscatter-related Ångström exponents are shown in Fig. 6.7. Mean extinction and backscatter-related $\mathring{A}^{355/532}$ range between -0.5 and 3 and -0.5 and 1.5, respectively. In dust layers the mean $\mathring{A}$ is generally smaller than in the MBL, an exception is the upper layer on 30 April. In this layer, small soot particles cause a high $\mathring{A}_{bsc}^{355/532}$. In the dried marine layer, the Ångström exponents are around 1, they are significantly higher than marine values on the same day, indicating smaller particles, but do not show a clear difference to other MBL mean values.

Mean values of MBL and elevated layer measurements are consistent with previous studies [*Tesche et al.*, 2011a; *Groß et al.*, 2011]. A difference between northern and southern latitudes and the dust-influenced region west of the Saharan dessert could be detected. Whereas the northern hemisphere is influenced by anthropogenic pollution, southern latitudes are more likely to be only marine influenced. Nevertheless, pure marine conditions, not influenced by aerosol originating from the continent, are rare and could only be observed at the end of PS95 near South Africa. Dried marine layers, characterised by a sharp increase of the particle depolarisation, were observed during both cruises. The particle depolarisation ratio in these layers range between 4–9% and are in good agreement with previous observations [*Murayama et al.*, 1999; *Sakai et al.*, 2000, 2010]. A clear difference of the dried marine layers in lidar ratio and Ångström exponent mean values to MBL measurements could not be observed.

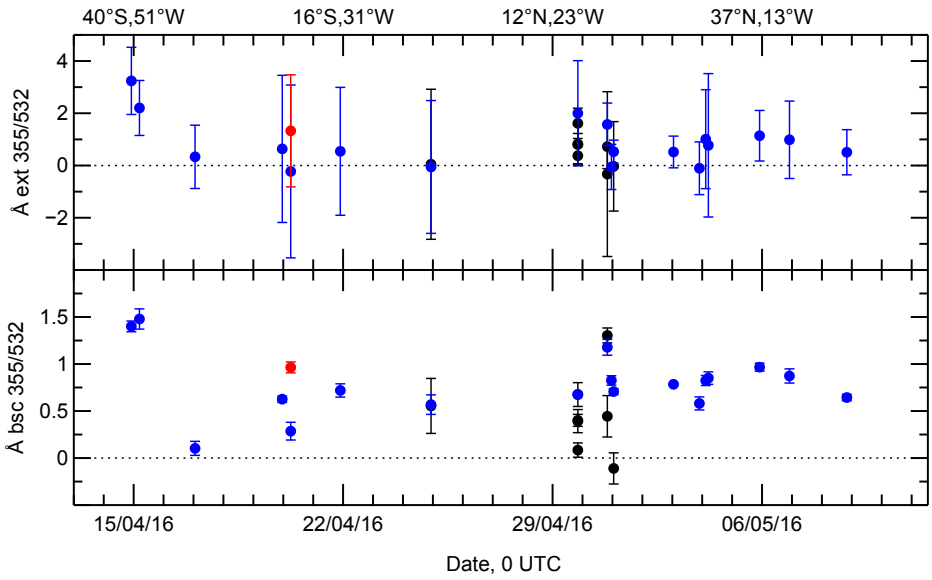


**Figure 6.7:** Same as Fig. 6.4 but for PS98.

## 6.2 Potential for particle typing

Mean values of lidar ratio, depolarisation ratio and Ångström exponent of all MBL and elevated aerosol layers shown in Sec. 6.1 and the dried marine layers on 30 November 2015 and 20 April 2016 are illustrated against each other to show differences in particle properties and illustrate the potential of aerosol classification using intensive quantities. Error bars were omitted for the sake of clarity. The backscatter-related Ångström exponent at 532/1064 nm could only be used from the PS95 measurements because of the not working 1064 nm channel during the PS98 cruise.

In Fig. 6.8, the lidar ratio at 355 nm (532 nm) is plotted against the particle depolarisation ratio at 355 nm (532 nm). A clear separation of marine and dust influenced MBL measurements can be seen. Pure marine MBL measurements show lidar ratios between 12 sr and 40 sr and particle depolarisation ratios less than 2.5%, whereas the particle depolarisation ratio of dust influenced MBL measurements ranges between 5–20%, caused by a significant amount of depolarising particles in the MBL. The lidar ratio of these layers also show a tendency to higher lidar ratios, caused by the mixing with dust particles. Elevated aerosol layer measurements can be divided into layers with a high particle depolarisation ratio (20–30%) and a lidar ratio of about 50–60 sr, layers with a lidar ratio between 30 sr and 75 sr and a lower particle depolarisation ratio and layers with a high lidar ratio (>60 sr) and a low particle depolarisation ratio (<10%). First are considered as pure dust cases, whereas the mixing with other non-depolarising particles lower the depolarisation ratio in the second category. These particles could be spherical marine particles or biomass-burning aerosol. Is the lidar ratio higher than reference values of pure dust (≈55 sr), the aerosol is considered to be soot, a lower lidar ratio indicate a mixture with marine particles. Layers with lidar ratios greater than 80 sr and a particle depolarisation lower than 10% are considered as smoke. This separation is illustrated in the lower panel of Fig. 6.8. MBL mixture represent the MBL cases with a significant amount of depolarising particles. Dusty mixtures are elevated aerosol layers consisting of dust and other non-depolarising particles.

Figure 6.9 illustrates the lidar ratio at 355 nm and 532 nm against the backscatter and extinction-related Ångström exponents at 355/532 nm and backscatter-related Ångström exponent at 532/1064 nm. A clear separation of MBL and elevated aerosol layer measurements can be seen, this separations is mainly caused by the lidar ratio whereas the Ångström exponent varies between 0.5 and 2 in MBL as well as in elevated layers.

In Fig. 6.10, the backscatter and extinction-related Ångström exponents at 355/532 nm and backscatter-related Ångström exponent at 532/1064 nm are illustrated as a function of the particle depolarisation ratio at 355 nm (right column) and at 532 nm (left column). Again, a separation of marine cases ($\delta^{par}$ <5%) and aerosol mixtures in the MBL (5%< $\delta^{par}$ <20%) can be seen at both depolarisation wavelengths and all Ångström exponents. At both depolarisation wavelengths, a slight tendency of the elevated aerosol layer measurements towards negative $\mathring{A}_{bsc}^{355/532}$ with increasing depolarisation values can be seen. It can be speculated, that negative backscatter-related Ångström exponents are related with a high amount of dust particles in the layer.

The $\mathring{A}_{ext}^{355/532}$ at both depolarisation wavelengths is more widely dispersed than the backscatter-related, but show similar patterns. In the illustration of $\mathring{A}_{bsc}^{532/1064}$ against the particle depolarisation ratio at 532 nm no tendency to smaller Ångström exponents with higher depolarisation ratio of the elevated aerosol layers can be observed.

Resulting from the preceding investigations, the main indicator for particle classification is the lidar ratio together with the particle depolarisation ratio. The backscatter and extinction-related Ångström exponent is relatively variable. A clear tendency of the dried marine layers is not visible. More dried marine layer observations are required for a proper investigation of typical intensive quantities.

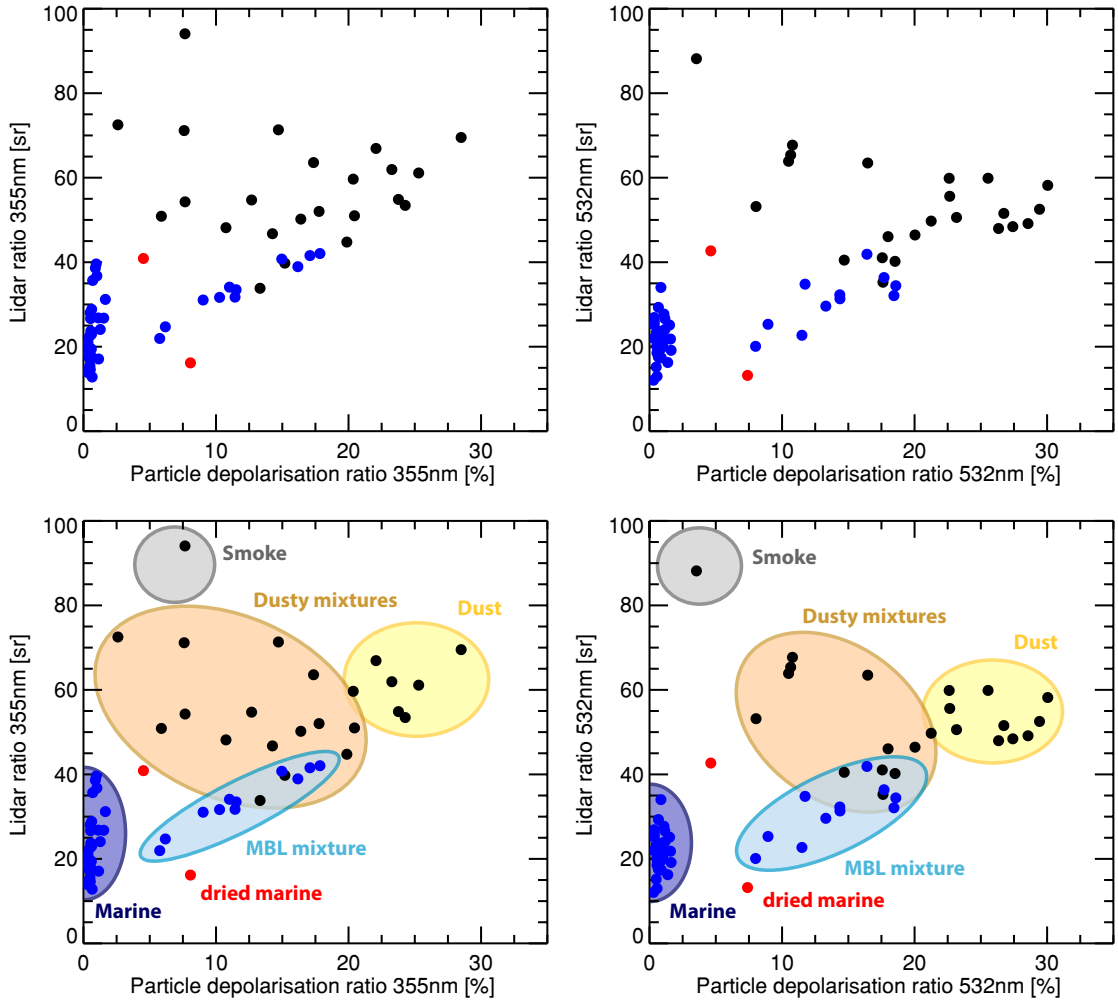


**Figure 6.8:** Upper panel: Lidar ratio as a function of the particle depolarisation ratio at 355 nm (left) and at 532 nm (right) from all analysed MBL (blue), elevated aerosol layer (black) and dried marine layer (red) measurements of PS95 and PS98. Lower panel: Same as the upper panel but with delineated aerosol classification.

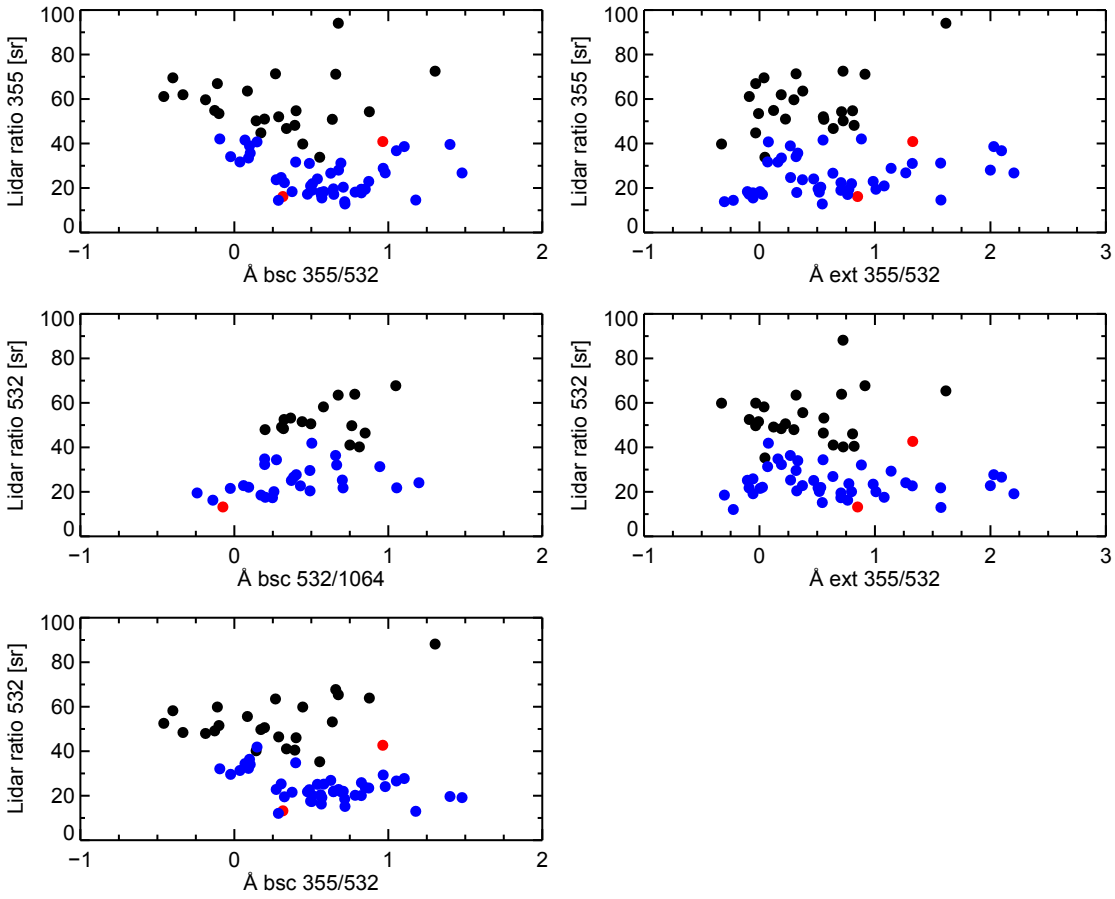


**Figure 6.9:** Lidar ratio at 355 nm (upper row) and 532 nm (second, third row) as a function of the backscatter-related Ångström exponent at 355/532 nm and 532/1064 nm (left column) and extinction-related Ångström exponent at 355/532 nm (right column). Blue dots represent MBL measurements, black dots elevated aerosol layers and red dots dried marine layers from PS95 and PS98.

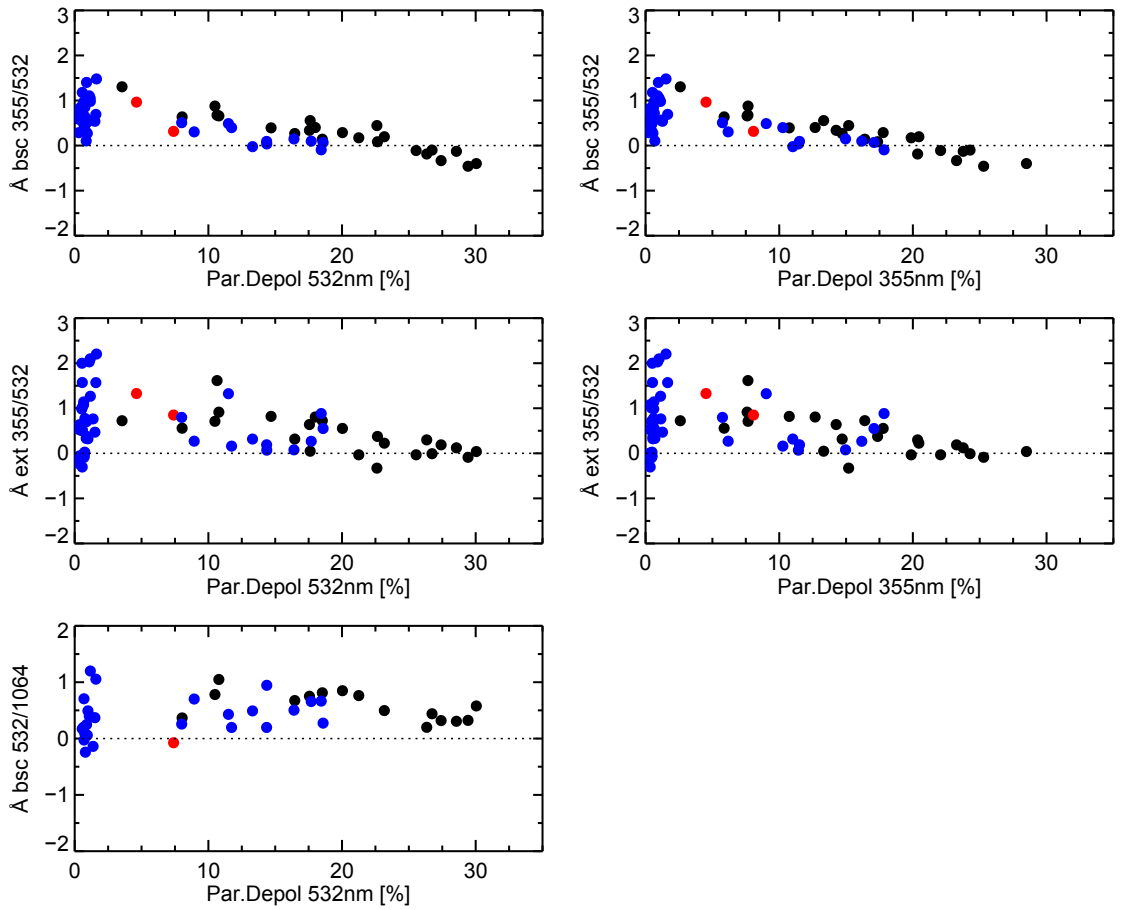


**Figure 6.10:** Backscatter and extinction-related Ångström exponents at 355/532 nm (first and second row) and backscatter-related Ångström exponent at 532/1064 nm (third row) as a function of the particle depolarisation ratio at 355 nm (right column) and at 532 nm (left column). Blue dots represent MBL measurements, black dots elevated aerosol layers and red dots dried marine layers from PS95 and PS98.

# Chapter 7

# Summary and conclusion

Multiwavelength Raman lidars of type Polly$^{XT}$ have been regularly operated on expeditions across the Atlantic Ocean aboard the research vessel Polarstern. In this work, lidar measurements from five Polarstern cruises across the Atlantic were presented. Two cruises, PS95 from Bremerhaven to Cape Town in autumn 2015 and PS98 from Punta Arenas to Bremerhaven in spring 2016, were analysed in detail. Due to the latest setup of Polly$^{XT}$-OCEANET, with near-range channels at four wavelengths, the investigation of the aerosol conditions within the MBL was possible for the first time.

Three case studies were presented. Marine conditions could be observed near South Africa at the end of PS95. Within the MBL, lidar ratios of around 23 sr at 355 nm and 532 nm were determined. The particle depolarisation ratio was around zero in the MBL and showed a sharp increase at both wavelengths on the top of the MBL before it decreased to around zero again. This peak in the particle depolarisation ratio is caused by marine aerosol which got non-spherical at low relative humidities. There are only a few observations of such dried marine aerosol layers above the MBL, this study therefore represents a valuable addition to previous studies.

On 11 November 2015, an almost pure dust plume could be observed. The 532 nm backscatter coefficient in the observed layer was significantly larger than the 355 nm signal resulting in a higher lidar ratio at 355 nm (61±4 sr) than at 532 nm (53±2 sr) and a negative backscatter-related Ångström exponent of $-0.4 \pm 0.1$ at 355/532 nm. The height-constant particle depolarisation ratio account 29±1% at 532 nm and 25±1% at 355 nm. The MBL was partly mixed with dust according to the higher lidar ratio of 30 sr at both wavelengths and particle depolarisation ratios of 6% and 9% at 355 nm and 532 nm, respectively.

Layers of Saharan dust partly mixed with biomass-burning smoke were observed near the Cape Verde Islands in spring 2016. Four layers with different fractions of dust and biomass-burning aerosol were detected resulting from different transport paths of the aerosol particles in the individual altitudes. At the same time, the MBL consists of only marine aerosol indicated by depolarisation ratios around zero at both wavelengths and a lidar ratio of 22±1 sr at 355 nm.

In addition to the optical properties in lofted layers, which are in good agreement with for-

mer campaigns, e.g. SAMUM [*Tesche et al.*, 2011a; *Groß et al.*, 2011; *Freudenthaler et al.*, 2009] or ship-borne observations over the Atlantic Ocean [*Kanitz et al.*, 2013; *Rittmeister*, 2015], an intense analysis of the underlying MBL could be made. Therefore almost the whole troposphere above the Atlantic Ocean could be characterized with respect to aerosols.
Additionally, a statistical analysis has been performed to illustrate latitudinal trends and the potential of aerosol classification from these ship cruises. 27 measurements were selected to represent the temporal trend of the aerosol optical properties during PS95 (Bremerhaven–Cape Town, autumn 2015). Latitudinal differences in the optical properties within the MBL, caused by the downmixing of dust in the tropics and anthropogenic influences in the northern latitudes, were observed. In the southern hemisphere, the optical properties of the MBL correlate with typical marine values. The MBL measurements on PS98 (Punta Arenas–Bremerhaven, spring 2016) did not show such a significant latitudinal trend as on PS95. No clear indications of dust mixed into the MBL were found. On both cruises, elevated aerosol layers were mainly observed in the northern tropics. Dried marine layers above the top of the MBL could be observed on one day on PS95 as well as PS98. The particle depolarisation ratio of all observed dried marine layers ranged between 4–9% indicating non-sphericity of the particles. Ångström exponent and lidar ratio did not show clear tendencies. More marine cases with an overlying dried marine layer would be necessary for a proper investigation of their optical properties.
All 45 night measurements from PS95 and PS98 were used to illustrate dependencies between lidar ratio, particle depolarisation ratio and Ångström exponent. Lidar ratio and particle depolarisation ratio have been found to be the main indicator for the particle type, whereas the Ångström exponent is rather variable.
Shipborne measurements present an important addition to campaigns and permanent stations on land and improve the knowledge of aerosol conditions in regions were observations are rare, e.g. in the southern Atlantic. The collected data can be used to validate model calculations (e.g. DREAM, MACC, SKIRON) or spaceborne observations (e.g. CALIPSO, EARTHCARE). Nevertheless, more data is required for a more detailed latitudinal investigation of tropospheric aerosol. Especially for the investigation of the MBL and the influence of dried marine aerosol, more ship-borne measurements are necessary. In the future, the OCEANET facility, including Polly$^{XT}$, will be operated on more Polarstern expeditions across the Atlantic and in the Arctic and will further enlarge the dataset of vertical profiles over the oceans.

# Bibliography

Albrecht, B. A. (1989), Aerosols, cloud microphysics, and fractional cloudiness, *Science*, *245*, 1227–1230, doi:10.1126/science.245.4923.1227.

Althausen, D., R. Engelmann, H. Baars, B. Heese, A. Ansmann, D. Müller, and M. Komppula (2009), Portable Raman lidar Polly$^{XT}$ for automated profiling of aerosol backscatter, extinction, and depolarization, *Journal of Atmospheric and Oceanic Technology*, *26*, 2366–2378, doi:10.1175/2009JTECHA1304.1.

Andreae, M. O. (1991), Biomass burning: Its history, use and distribution and its impact on environmental quality and global climate, in *Global Biomass Burning: Atmospheric, Climatic and Biospheric Implications*, edited by J. S. Levine, pp. 3–21, MIT Press, Cambridge, Mass.

Andreae, M. O., and H. Raemdonck (1983), Dimethyl Sulfide in the Surface Ocean and the Marine Atmosphere: A Global View, *Science*, *221*(4612), 744–747, doi:10.1126/science.221.4612.744.

Andreae, M. O., and D. Rosenfeld (2008), Aerosol-Cloud-Precipitation Interactions. Part 1. The Nature and Sources of Cloud-Active Aerosols, *Earth-Science Reviews*, *89*(1–2), 13–41, doi:10.1016/j.earscirev.2008.03.001.

Ångström, A. (1929), On the Atmospheric Transmission of Sun Radiation and on Dust in the Air, *Geografiska Annaler*, *11*, pp. 156-166.

Ansmann, A., and D. Müller (2005), Lidar and atmospheric aerosol particles, in *Lidar: Range–Resolved Optical Remote Sensing of the Atmosphere*, edited by C. Weitkamp, pp. 105–142, Springer.

Ansmann, A., M. Riebesell, and C. Weitkamp (1990), Measurement of atmospheric aerosol extinction profiles with a Raman lidar, *Optics Letters*, *15*, 746–748.

Ansmann, A., U. Wandinger, M. Riebesell, C. Weitkamp, and W. Michaelis (1992), Independent measurement of extinction and backscatter profiles in cirrus clouds by using a combined Raman elastic–backscatter lidar, *Applied Optics*, *31*, 7113–7131.

Ansmann, A., F. Wagner, D. Althausen, D. Müller, A. Herber, and U. Wandinger (2001), European pollution outbreaks during ACE 2: Lofted aerosol plumes observed with Raman lidar at the Portuguese coast, *Journal of Geophysical Research: Atmospheres*, *106*(D18), 20725–20733, doi:10.1029/2000JD000091.

Ansmann, A., H. Baars, M. Tesche, D. Müller, D. Althausen, R. Engelmann, T. Pauliquevis, and P. Artaxo (2009), Dust and smoke transport from Africa to South America: Lidar profiling over Cape Verde and the Amazon rainforest, *Geophysical Research Letters*, *36*(11), doi:10.1029/2009GL037923, l11802.

Antuña, J. C., E. Landulfo, B. Clemesha, F. Zaratti, E. Quel, A. Bastidas, R. Estevan, and B. Barja (2012), Lidar community in Latin America: a decade of challenges and successes, in *Reviewed and Revised Papers of the 26th International Laser Radar Conference*, pp. 25–29.

Baars, H., A. Ansmann, D. Althausen, R. Engelmann, P. Artaxo, T. Pauliquevis, and R. Souza (2011), Further evidence for significant smoke transport from Africa to Amazonia, *Geophysical Research Letters*, *38*(20), doi:10.1029/2011GL049200, l20802.

Baars, H., A. Ansmann, D. Althausen, R. Engelmann, B. Heese, D. Müller, P. Artaxo, M. Paixao, T. Pauliquevis, and R. Souza (2012), Aerosol profiling with lidar in the Amazon Basin during the wet and dry season, *Journal of Geophysical Research: Atmospheres*, *117*(D21), doi:10.1029/2012JD018338, d21201.

Baars, H., T. Kanitz, R. Engelmann, D. Althausen, B. Heese, M. Komppula, J. Preißler, M. Tesche, A. Ansmann, U. Wandinger, J.-H. Lim, J. Y. Ahn, I. S. Stachlewska, V. Amiridis, E. Marinou, P. Seifert, J. Hofer, A. Skupin, F. Schneider, S. Bohlmann, A. Foth, S. Bley, A. Pfüller, E. Giannakaki, H. Lihavainen, Y. Viisanen, R. K. Hooda, S. N. Pereira, D. Bortoli, F. Wagner, I. Mattis, L. Janicka, K. M. Markowicz, P. Achtert, P. Artaxo, T. Pauliquevis, R. A. F. Souza, V. P. Sharma, P. G. van Zyl, J. P. Beukes, J. Sun, E. G. Rohwer, R. Deng, R.-E. Mamouri, and F. Zamorano (2016), An overview of the first decade of Polly$^{\mathrm{NET}}$: an emerging network of automated Raman-polarization lidars for continuous aerosol profiling, *Atmospheric Chemistry and Physics*, *16*(8), 5111–5137, doi:10.5194/acp-16-5111-2016.

Barbosa, H. M. J., F. J. S. Lopes, A. Silva, D. Nisperuza, B. Barja, P. Ristori, D. A. Gouveia, C. Jimenez, E. Montilla, G. L. Mariano, E. Landulfo, A. Bastidas, and E. J. Quel (2014), The first ALINE measurements and intercomparison exercise on lidar inversion algorithms, *Optica pura y aplicada*, *47*(2), 99–108, doi:10.7149/OPA.47.2.109.

Ben-Ami, Y., I. Koren, Y. Rudich, P. Artaxo, S. T. Martin, and M. O. Andreae (2010), Transport of North African dust from the Bodl depression to the Amazon Basin: a case study, *Atmospheric Chemistry and Physics*, *10*(16), 7533–7544, doi:10.5194/acp-10-7533-2010.

Bösenberg, J., R. Hoff, A. Ansmann, D. Müller, J. C. Antuña, D. Whiteman, N. Sugimoto, A. Apituley, M. Hardesty, J. Welton, E. Eloranta, Y. Arshinov, S. Kinne, and V. Freudenthaler (2007), Plan for the implementation of the GAW Aerosol Lidar Observation Network GALION, *GAW No. 178*.

Bucholtz, A. (1995), Rayleigh–scattering calculations for the terrestrial atmosphere, *Applied Optics*, *34*, 2765–2773.

Chaikovsky, A., A. Ivanov, Y. Balin, A. Elnikov, G. Tulinov, I. Plusnin, O. Bukin, and B. Chen (2006), Lidar network CIS-LiNet for monitoring aerosol and ozone in CIS regions, *Proc. SPIE*, *6160*, 616035-616035-9, doi:10.1117/12.675920.

Eck, T. F., B. N. Holben, J. S. Reid, O. Dubovik, A. Smirnov, N. T. O'Neill, I. Slutsker, and S. Kinne (1999), Wavelength dependence of the optical depth of biomass burning, urban, and desert dust aerosols, *Journal of Geophysical Research: Atmospheres*, *104*(D24), 31333–31349, doi:10.1029/1999JD900923.

Engelmann, R., T. Kanitz, H. Baars, B. Heese, D. Althausen, A. Skupin, U. Wandinger, M. Komppula, I. S. Stachlewska, V. Amiridis, E. Marinou, I. Mattis, H. Linné, and A. Ansmann (2016), The automated multiwavelength Raman polarization and water-vapor lidar Polly$^{XT}$: the neXT generation, *Atmospheric Measurement Techniques*, *9*(4), 1767–1784, doi:10.5194/amt-9-1767-2016.

Fernald, F. G. (1984), Analysis of atmospheric lidar observations: some comments, *Applied Optics*, *23*, 652–653.

Freudenthaler, V. (2016), About the effects of polarising optics on lidar signals and the $\Delta 90$ calibration, *Atmospheric Measurement Techniques*, *9*(9), 4181–4255, doi:10.5194/amt-9-4181-2016.

Freudenthaler, V., M. Esselborn, M. Wiegner, B. Heese, M. Tesche, A. Ansmann, D. Müller, D. Althausen, M. Wirth, A. Fix, G. Ehret, P. Knippertz, C. Toledano, J. Gasteiger, M. Garhammer, and M. Seefeldner (2009), Depolarization ratio profiling at several wavelengths in pure Saharan dust during SAMUM 2006, *Tellus Series B*, *61*, 165–179.

Giannakaki, E., A. Pfüller, K. Korhonen, T. Mielonen, L. Laakso, V. Vakkari, H. Baars, R. Engelmann, J. P. Beukes, P. G. Van Zyl, M. Josipovic, P. Tiitta, K. Chiloane, S. Piketh, H. Lihavainen, K. E. J. Lehtinen, and M. Komppula (2015), One year of Raman lidar observations of free-tropospheric aerosol layers over South Africa, *Atmospheric Chemistry and Physics*, *15*(10), 5429–5442, doi:10.5194/acp-15-5429-2015.

Groß, S., M. Tesche, V. Freudenthaler, C. Toledano, M. Wiegner, A. Ansmann, D. Althausen, and M. Seefeldner (2011), Characterization of Saharan dust, marine aerosols and mixtures of biomass–burning aerosols and dust by means of multi–wavelength depolarization and Raman lidar measurements during SAMUM 2, *Tellus B*, *63*(4), doi:10.1111/j.1600-0889.2011.00556.x.

Heintzenberg, J. (2009), The SAMUM-1 experiment over Southern Morocco: overview and introduction, *Tellus B*, *61*(1), 2–11, doi:10.1111/j.1600-0889.2008.00403.x.

Hoff, R. M., K. J. McCann, B. Demoz, J. Reichardt, D. N. Whiteman, T.McGee, M. P. McCormick, C. R. Philbrick, K. Strawbridge, F. Moshary, B. Gross, S. Ahmed, D. Venable, and E. Joseph (2002), Regional East Atmospheric Lidar Mesonet: REALM , in *Lidar Remote Sensing in Atmospheric and Earth Sciences* , edited by L. Bissonette, G. Roy, and G. Valle, pp. 281–284, Def. R&D Can. Valcartier.

Illingworth, A. J., H. W. Barker, A. Beljaars, M. Ceccaldi, H. Chepfer, N. Clerbaux, J. Cole, J. Delanoë, C. Domenech, D. P. Donovan, S. Fukuda, M. Hirakata, R. J. Hogan, A. Huenerbein, P. Kollias, T. Kubota, T. Nakajima, T. Y. Nakajima, T. Nishizawa, Y. Ohno, H. Okamoto, R. Oki, K. Sato, M. Satoh, M. W. Shephard, A. Velázquez-Blázquez, U. Wandinger, T. Wehr, and G.-J. van Zadelhoff (2015), The EarthCARE Satellite: The Next Step Forward in Global Measurements of Clouds, Aerosols, Precipitation, and Radiation, *Bull. Amer. Meteor. Soc.*, *96*, 1311–1332, doi:10.1175/BAMS-D-12-00227.1.

IPCC (2013), *Climate Change 2013: The Physical Science Basis. Contribution of Working Group I to the Fifth Assessment Report of the Intergovernmental Panel on Climate Change*, Cambridge University Press, 589 pp.

Janicka, L., I. S. Stachlewska, K. M. Markowicz, H. Baars, R. Engelmann, and B. Heese (2016), Lidar Measurements of Canadian Forest Fire Smoke Episode Observed in July 2013 over Warsaw, Poland, *EPJ Web of Conferences*, *119*, 18005, doi:10.1051/epjconf/201611918005.

Kandler, K., L. Schütz, C. Deutscher, M. Ebert, H. Hofmann, S. Jäckel, R. Jaenicke, P. Knippertz, K. Lieke, A. Massling, A. Petzold, A. Schladitz, B. Weinzierl, A. Wiedensohler, S. Zorn, and S. Weinbruch (2009), Size distribution, mass concentration, chemical and mineralogical composition and derived optical parameters of the boundary layer aerosol at Tinfou, Morocco, during SAMUM 2006, *Tellus B*, *61*(1), 32–50, doi:10.1111/j.1600-0889.2008.00385.x.

Kanitz, T. (2012), Vertical distribution of aerosols above the Atlantic Ocean, Punta Arenas (Chile), and Stellenbosch (South Africa). Characterization, solar radiative effects and ice nucleating properties, Ph.D. thesis, Technische Universität Berlin, available at: `http://www.tropos.de/en/institute/departments/remote-sensing-of-atmospheric-processes-new/ground-based-remote-sensing/academical-degrees/`.

Kanitz, T., A. Ansmann, R. Engelmann, and D. Althausen (2013), North-south cross sections of the vertical aerosol distribution over the Atlantic Ocean from multiwavelength Raman/polarization lidar during Polarstern cruises, *Journal of Geophysical Research: Atmospheres*, *118*(6), 2643–2655, doi:10.1002/jgrd.50273.

Kanitz, T., R. Engelmann, B. Heinold, H. Baars, A. Skupin, and A. Ansmann (2014), Tracking the Saharan Air Layer with shipborne lidar across the tropical Atlantic, *Geophysical Research Letters*, *41*(3), 1044–1050, doi:10.1002/2013GL058780.

Klett, J. D. (1981), Stable analytical solution for processing lidar returns, *Applied Optics*, *20*, 211–220.

Kokhanovsky, A. (2008), *Aerosol Optics: Light Absorption and Scattering by Particles in the Atmosphere*, Springer Praxis Books, Springer Berlin Heidelberg.

König-Langlo, G. (2016), Upper air soundings during POLARSTERN cruise PS98 (ANT-XXXI/4), doi:10.1594/PANGAEA.861660.

Leblanc, T., R. J. Sica, J. A. E. van Gijsel, S. Godin-Beekmann, A. Haefele, T. Trickl, G. Payen, and F. Gabarrot (2016), Proposed standardized definitions for vertical resolution and uncertainty in the NDACC lidar ozone and temperature algorithms – Part 1: Vertical resolution, *Atmospheric Measurement Techniques*, *9*(8), 4029–4049, doi:10.5194/amt-9-4029-2016.

Mattis, I. (2002), Aufbau eines Feuchte–Temperatur–Aerosol–Ramanlidars und Methodenentwicklung zur kombinierten Analyse von Trajektorien und Aerosolprofilen, Ph.D. thesis, Leipzig University, available at: `http://www.tropos.de/en/institute/departments/remote-sensing-of-atmospheric-processes-new/ground-based-remote-sensing/academical-degrees/`.

Müller, D., U. Wandinger, and A. Ansmann (1999), Microphysical particle parameters from extinction and backscatter lidar data by inversion with regularization: theory, *Appl. Opt.*, *38*(12), 2346–2357, doi:10.1364/AO.38.002346.

Müller, D., I. Mattis, U. Wandinger, A. Ansmann, D. Althausen, and A. Stohl (2005), Raman lidar observations of aged Siberian and Canadian forest fire smoke in the free troposphere over Germany in 2003: Microphysical particle characterization, *Journal of Geophysical Research*, *110*, D17201, doi:10.1029/2004JD005756.

Müller, D., A. Ansmann, I. Mattis, M. Tesche, U. Wandinger, D. Althausen, and G. Pisani (2007), Aerosol–type–dependent lidar ratios observed with Raman lidar, *Journal of Geophysical Research: Atmospheres*, *112*, D16202, doi:10.1029/2006JD008292.

Müller, T., A. Schladitz, A. Massling, N. Kaaden, K. Kandler, and A. Wiedensohler (2009), Spectral absorption coefficients and imaginary parts of refractive indices of Saharan dust during SAMUM-1, *Tellus B*, *61*(1).

Murayama, T., H. Okamoto, N. Kaneyasu, H. Kamataki, and K. Miura (1999), Application of lidar depolarization measurement in the atmospheric boundary layer: Effects of dust and sea-salt particles, *Journal of Geophysical Research: Atmospheres*, *104*(D24), 31781–31792, doi:10.1029/1999JD900503.

Myhre, G., B. H. Samset, M. Schulz, Y. Balkanski, S. Bauer, T. K. Berntsen, H. Bian, N. Bellouin, M. Chin, T. Diehl, R. C. Easter, J. Feichter, S. J. Ghan, D. Hauglustaine, T. Iversen, S. Kinne, A. Kirkevåg, J.-F. Lamarque, G. Lin, X. Liu, M. T. Lund, G. Luo, X. Ma, T. van Noije, J. E. Penner, P. J. Rasch, A. Ruiz, Ø. Seland, R. B. Skeie, P. Stier, T. Takemura, K. Tsigaridis, P. Wang, Z. Wang, L. Xu, H. Yu, F. Yu, J.-H. Yoon, K. Zhang, H. Zhang, and C. Zhou (2013), Radiative forcing of the direct aerosol effect from AeroCom Phase II simulations, *Atmospheric Chemistry and Physics*, *13*(4), 1853–1877, doi:10.5194/acp-13-1853-2013.

Nisantzi, A., R. E. Mamouri, A. Ansmann, and D. Hadjimitsis (2014), Injection of mineral dust into the free troposphere during fire events observed with polarization lidar at Limassol, Cyprus, *Atmospheric Chemistry and Physics*, *14*(22), 12155–12165, doi:10.5194/acp-14-12155-2014.

Ocko, I. B., V. Ramaswamy, P. Ginoux, Y. Ming, and L. W. Horowitz (2012), Sensitivity of scattering and absorbing aerosol direct radiative forcing to physical climate factors, *Journal of Geophysical Research: Atmospheres*, *117*(D20), doi:10.1029/2012JD018019, d20203.

Pappalardo, G., A. Amodeo, A. Apituley, A. Comeron, V. Freudenthaler, H. Linné, A. Ansmann, J. Bösenberg, G. D'Amico, I. Mattis, L. Mona, U. Wandinger, V. Amiridis, L. Alados-Arboledas, D. Nicolae, and M. Wiegner (2014), EARLINET: towards an advanced sustainable European aerosol lidar network, *Atmospheric Measurement Techniques*, *7*(8), 2389–2409, doi:10.5194/amt-7-2389-2014.

Preiler, J., F. Wagner, J. L. Guerrero-Rascado, and A. M. Silva (2013), Two years of free-tropospheric aerosol layers observed over Portugal by lidar, *Journal of Geophysical Research: Atmospheres*, *118*(9), 3676–3686, doi:10.1002/jgrd.50350.

Prospero, J. M. (2002), The Chemical and Physical Properties of Marine Aerosols: An Introduction, in *Chemistry of Marine Water and Sediments*, edited by A. Gianguzza, E. Pelizzetti, and S. Sammartano, pp. 35–82, Springer Berlin Heidelberg, doi:10.1007/978-3-662-04935-8_2.

Rittmeister, F. (2015), The African dust and smoke layer over the tropical Atlantic during the spring season 2013: Ship-based lidar observations from Guadeloupe to Cape Verde., Master's thesis, Leipzig University, available at: `http://www.tropos.de/en/institute/departments/remote-sensing-of-atmospheric-processes-new/ground-based-remote-sensing/academical-degrees/`.

Russell, P. B., P. V. Hobbs, and L. L. Stowe (1999), Aerosol properties and radiative effects in the United States East Coast haze plume: An overview of the Tropospheric Aerosol Radiative Forcing Observational Experiment (TARFOX), *Journal of Geophysical Research: Atmospheres*, *104*(D2), 2213–2222, doi:10.1029/1998JD200028.

Sakai, T., T. Shibata, S.-A. Kwon, Y.-S. Kim, K. Tamura, and Y. Iwasaka (2000), Free tropospheric aerosol backscatter, depolarization ratio, and relative humidity measured with the Raman lidar at Nagoya in 1994–1997: contributions of aerosols from the Asian Continent and the Pacific Ocean, *Atmospheric Environment*, *34*(3), 431–442, doi:10.1016/S1352-2310(99)00328-3.

Sakai, T., T. Nagai, Y. Zaizen, and Y. Mano (2010), Backscattering linear depolarization ratio measurements of mineral, sea-salt, and ammonium sulfate particles simulated in a laboratory chamber, *Appl. Opt.*, *49*(23), 4441–4449, doi:10.1364/AO.49.004441.

Saltzman, E. S. (2009), Marine Aerosols, in *Surface Ocean-Lower Atmosphere Processes*, edited by C. L. Quéré and E. S. Saltzman, pp. 17–35, American Geophysical Union, Washington, D. C., doi:10.1029/2008GM000769.

Sasano, Y., E. V. Browell, and S. Ismail (1985), Error caused by using a constant extinction/backscattering ratio in the lidar solution, *Appl. Opt.*, *24*(22), 3929–3932, doi:10.1364/AO.24.003929.

Seifert, P., A. Ansmann, I. Mattis, U. Wandinger, M. Tesche, R. Engelmann, D. Müller, C. PéRez, and K. Haustein (2010), Saharan dust and heterogeneous ice formation: Eleven years of cloud observations at a central European EARLINET site, *Journal of Geophysical Research (Atmospheres)*, *115*, D20201, doi:10.1029/2009JD013222.

Smirnov, A., B. Holben, Y. Kaufman, O. Dubovik, T. Eck, I. Slutsker, C. Pietras, and R. Halthore (2002), Optical Properties of Atmospheric Aerosol in Maritime Environments, *Journal of the Atmospheric Sciences*, *59*(3), 501–523, doi:10.1175/1520-0469(2002)059⟨0501:OPOAAI⟩2.0.CO;2.

Smirnov, A., B. N. Holben, I. Slutsker, D. M. Giles, C. R. McClain, T. F. Eck, S. M. Sakerin, A. Macke, P. Croot, G. Zibordi, P. K. Quinn, J. Sciare, S. Kinne, M. Harvey, T. J. Smyth, S. Piketh, T. Zielinski, A. Proshutinsky, J. I. Goes, N. B. Nelson, P. Larouche, V. F. Radionov, P. Goloub, K. Krishna Moorthy, R. Matarrese, E. J. Robertson, and F. Jourdin (2009), Maritime Aerosol Network as a component of Aerosol Robotic Network, *Journal of Geophysical Research: Atmospheres*, *114*(D6), doi:10.1029/2008JD011257, d06204.

Stein, A. F., R. R. Draxler, G. D. Rolph, B. J. B. Stunder, and M. D. Cohen (2015), NOAA's HYSPLIT Atmospheric Transport and Dispersion Modeling System, *Bulletin of the American Meteorological Society*, *96*(12), 2059-2077, doi:10.1175/BAMS-D-14-00110.1.

Sugimoto, N., I. Matsui, A. Shimizu, T. Nishizawa, Y. Hara, C. Xie, I. Uno, K. Yumimoto, Z. Wang, and S.-C. Yoon (2008), Lidar network observations of tropospheric aerosols, *Lidar Remote Sensing for Environmental Monitoring IX, Proc. SPIE*, *7153*, 71530A-71530A-13, doi:10.1117/12.806540.

Swap, R., M. Garstang, S. A. Macko, P. D. Tyson, W. Maenhaut, P. Artaxo, P. Kllberg, and R. Talbot (1996), The long-range transport of southern African aerosols to the tropical South Atlantic, *Journal of Geophysical Research: Atmospheres*, *101*(D19), 23777–23791, doi:10.1029/95JD01049.

Tesche, M., A. Ansmann, D. Müller, D. Althausen, R. Engelmann, V. Freudenthaler, and S. Groß (2009a), Vertically resolved separation of dust and smoke over Cape Verde using multiwavelength Raman and polarization lidars during Saharan Mineral Dust Experiment 2008, *Journal of Geophysical Research*, *114*, D13202, doi:10.1029/2009JD011862.

Tesche, M., A. Ansmann, D. Müller, D. Althausen, I. Mattis, B. Heese, V. Freudenthaler, M. Wiegner, M. Esselborn, G. Pisani, and P. Knippertz (2009b), Vertical profiling of Saharan dust with Raman lidars and airborne HSRL in southern Morocco during SAMUM, *Tellus Series B*, *61*, 144–164.

Tesche, M., S. Groß, A. Ansmann, D. Müller, D. Althausen, V. Freudenthaler, and M. Esselborn (2011a), Profiling of Saharan dust and biomass-burning smoke with multiwavelength polarization Raman lidar at Cape Verde, *Tellus B*, *63*(4).

Tesche, M., D. Müller, S. Groß, A. Ansmann, D. Althausen, V. Freudenthaler, B. Weinzierl, A. Veira, and A. Petzold (2011b), Optical and microphysical properties of smoke over Cape Verde inferred from multiwavelength lidar measurements, *Tellus B*, *63*(4), 677–694, doi:10.1111/j.1600-0889.2011.00549.x.

Twomey, S. (1977), The Influence of Pollution on the Shortwave Albedo of Clouds, *Journal of Atmospheric Science*, *34*(7), 1149–1154.

Veselovskii, I., P. Goloub, T. Podvin, V. Bovchaliuk, Y. Derimian, P. Augustin, M. Fourmentin, D. Tanre, M. Korenskiy, D. N. Whiteman, A. Diallo, T. Ndiaye, A. Kolgotin, and O. Dubovik (2016), Retrieval of optical and physical properties of African dust from multiwavelength Raman lidar measurements during the SHADOW campaign in Senegal, *Atmospheric Chemistry and Physics*, *16*(11), 7013–7028, doi:10.5194/acp-16-7013-2016.

Wandinger, U. (2005a), Introduction to Lidar, in *Lidar: Range–Resolved Optical Remote Sensing of the Atmosphere*, edited by C. Weitkamp, pp. 1–18, Springer.

Wandinger, U. (2005b), Raman Lidar, in *Lidar: Range-Resolved Optical Remote Sensing of the Atmosphere*, edited by C. Weitkamp, pp. 241–267, Springer.

Wandinger, U., and A. Ansmann (2002), Experimental determination of the lidar overlap profile with Raman lidar, *Applied Optics*, *41*, 511–514.

Weinzierl, B., A. Ansmann, J. Prospero, D. Althausen, N. Benker, F. Chouza, M. Dollner, D. Farrell, W. Fomba, V. Freudenthaler, J. Gasteiger, S. Groß, M. Haarig, B. Heinold, K. Kandler, T. Kristensen, O. Mayol-Bracero, T. Müller, O. Reitebuch, D. Sauer, A. Schfler, K. Schepanski, A. Spanu, I. Tegen, C. Toledano, and A. Walser (2016),

The Saharan Aerosol Long-range Transport and Aerosol-Cloud-Interaction Experiment (SALTRACE): overview and selected highlights., *Bulletin of the American Meteorological Society*, doi:10.1175/BAMS-D-15-00142.1, in press.

Welton, E., J. Campbell, J. Spinhirne, and V. Scott (2001), Global monitoring of clouds and aerosols using a network of micro-pulse lidar systems, in *Lidar remote sensing for industry and environment monitoring* , edited by U. Singh, T. Itabe, and N. Sugimoto, pp. 151–158, Proc. SPIE.

# List of Figures

1.1 Lidar stations on northern and southern hemisphere . . . . . 2

2.1 Aerosol sources and their expected transport direction over the Atlantic Ocean 6

3.1 Aerosol classification by measurements of lidar ratio and particle linear depolarisation ratio at 355 nm . . . . . 13

4.1 RV Polarstern and the OCEANET container . . . . . 16
4.2 Polarstern cruises with Polly$^{XT}$ aboard . . . . . 17
4.3 Optical setup of Polly$^{XT}$- OCEANET . . . . . 18
4.4 Illustration of the overlap effect . . . . . 19
4.5 Observational overview of ANT XXVII/4 . . . . . 24
4.6 Observational overview of ANT XXIX/1 . . . . . 25
4.7 Observational overview of PS83 . . . . . 26
4.8 Observational overview of PS95 . . . . . 27
4.9 Observational overview of PS98 . . . . . 28

5.1 Observational overview of the marine conditions during PS95 . . . . . 30
5.2 Profiles averaged for 30 November 2015, 01:15–02:30 UTC . . . . . 31
5.3 NOAA HYSPLIT backward trajectories ending at 30 November 2015, 02:00 UTC 32
5.4 NOAA HYSPLIT backward trajectories ending at 11 November 2015, 20:00 UTC and BSC DREAM Dust load . . . . . 33
5.5 Observational overview of the first dust event observed during PS95 . . . . . 34
5.6 Profiles averaged for 11 November 2015, 19:30–21:00 UTC . . . . . 35
5.7 Observational overview of the mixed layers during PS98 . . . . . 37
5.8 Profiles averaged for 29 April 2016, 20:15–21:00 UTC . . . . . 38
5.9 NOAA HYSPLIT backward trajectories ending at 29 April 2016, 21:00 UTC at the position of Polarstern and MODIS fire data . . . . . 39

6.1 MBL top height and extent of the elevated aerosol layers and the dried marine layers for PS95 and PS98 . . . . . 42
6.2 Mean values of the backscatter coefficient at 355 nm and 532 nm and the extinction coefficient at 355 nm and 532 nm for the analysed layers on PS95 . . 43

6.3 Mean values of the lidar ratio and the particle depolarisation ratio at 355 nm and 532 nm for the the analysed layers on PS95 . . . . . 44
6.4 Mean values of the extinction and backscatter-related Ångström exponents of the analysed layers on PS95. . . . . 45
6.5 Same as Fig. 6.2 but for PS98 for the layers shown in Fig. 6.1. . . . . 46
6.6 Same as Fig. 6.3 but for PS98. . . . . 47
6.7 Same as Fig. 6.4 but for PS98. . . . . 48
6.8 Lidar ratio as a function of the particle depolarisation ratio at 355 nm and 532 nm from all analysed layers on PS95 and PS98 . . . . . 50
6.9 Lidar ratio at 355 nm and 532 nm as a function of the backscatter and extinction-related Ångström exponents . . . . . 51
6.10 Backscatter and extinction-related Ångström exponents as a function of the particle depolarisation ratio at 355 nm and 532 nm . . . . . 52

# List of Tables

3.1 Aerosol optical properties derived in previous campaigns: lidar ratio $S$ at 355 nm and 532 nm, extinction-related 355/532 nm Ångström exponent and particle depolarisation ratio at 355 nm and 532 nm . . . . . 14

4.1 Previous Polarstern cruises with Polly$^{XT}$ aboard . . . . . 16

# List of Abbreviations

| | |
|---|---|
| ACE | North Atlantic Regional Aerosol Characterization |
| AD-NET | Asian Dust Network |
| AERONET | Aerosol Robotic Network |
| AGL | Above Ground Level |
| ALINE | American Lidar Network |
| ANT | Cruise label for Polarstern missions in the Antarctic region |
| AOT | Aerosol Optical Thickness |
| ARL | Air Resources Laboratory |
| AWI | Alfred Wegener Institute |
| BBA | Biomass Burning Aerosol |
| BHV | Bremerhaven |
| CALIPSO | Cloud–Aerosol Lidar and Infrared Pathfinder Satellite |
| CISLiNet | Commonwealth of Independent States Lidar Network |
| CLN | CREST Lidar Network |
| CREST | Cooperative Remote Sensing Science and Technology |
| CRH | Crystallization Relative Humidity |
| DMS | Dimethyl Sulphide |
| DREAM | Dust REgional Atmospheric Model |
| DRH | Deliquescence Relative Humidity |
| EARLINET | European Aerosol Research Lidar Network |
| EARTHCARE | Earth Clouds, Aerosols and Radiation Explorer |
| FR | Far-Range |
| GDAS | Global Data Assimilation System |
| GEOMAR | Helmholtz Centre for Ocean Research |
| HYSPLIT | Hybrid Single-Particle Lagrangian Integrated Trajectory |
| LIDAR | LIght Detection And Ranging |
| MACC | Monitoring Atmospheric Composition & Climate |
| MAN | Maritime Aerosol Network |
| MBL | Marine Boundary Layer |
| MODIS | Moderate Resolution Imaging Spectroradiometer |
| MPLNET | Micro-Pulse Lidar Network |
| NCEP | National Centers for Environmental Prediction |

| | |
|---|---|
| Nd:YAG | Neodymium-Doped Yttrium Aluminum Garnet |
| NDACC | Network for the Detection of Atmospheric Composition Change |
| NOAA | National Oceanic and Atmospheric Administration |
| NR | Near-Range |
| PMT | Photo Multiplier Tube |
| REALM | Regional East Aerosol Lidar Mesonet |
| RH | Relative Humidity |
| RV | Research Vessel |
| SALTRACE | Saharan Aerosol Long-range Transport and Aerosol-Cloud-Interaction Experiment |
| SAMUM | Saharan Mineral Dust Experiment |
| SHADOW | Study of SaHAran Dust Over West Africa |
| TROPOS | Leibniz Institute for Tropospheric Research |
| UTC | Universal Time Coordinated |

# Acknowledgement

I would like to thank everyone who supported and enabled this work.
First, I want to thank Prof. Dr. A. Macke and Dr. B. Pospichal for reviewing this master thesis.
Especially, I want to thank Holger Baars for the great supervision of my work and the time he spent on proof-reading and discussing further steps and ideas.
I also want to thank Ronny Engelmann for introducing me into the work with Polly$^{XT}$ on PS95 and his remote support day and night during PS98.
Thank you also to every member of the lidar group at TROPOS for always answering my questions and providing me with literature recommendations.
I am also thankful for the providing of additional data by the teams of BSC-DREAM8b, AERONET (MAN), HYSPLIT and GDAS.
A great thank you to the crews of the RV Polarstern for always helping me when I had technical problems or needed something and all scientists of PS95 and PS98 who made the time aboard Polarstern unforgettable.
Of course, I also have to thank my family and friends who supported and motivated me during my studies and especially this thesis.

# Selbstständigkeitserklärung

**Erklärung**

Ich versichere, dass ich die vorliegende Arbeit selbständig verfasst und keine anderen als die angegebenen Quellen und Hilfsmittel benutzt habe.
Alle Stellen, die wörtlich oder sinngemäß aus veröffentlichten oder noch nicht veröffentlichten Quellen entnommen sind, sind als solche kenntlich gemacht.
Die Zeichnungen oder Abbildungen in dieser Arbeit sind von mir selbst erstellt worden oder mit einem entsprechenden Quellennachweis versehen.
Diese Arbeit ist in gleicher oder ähnlicher Form noch bei keiner anderen Prüfungsbehörde eingereicht worden.

Leipzig, den 7. April 2017

---

Stephanie Bohlmann